Acta Materialia 231 (2022) 117859

Contents lists available at ScienceDirect

Acta Materialia

journal homepage: www.elsevier.com/locate/actamat

Full length article

Interactive effects of interfacial energy anisotropy and solute transport on solidification patterns of Al-Cu alloys

Ghavam Azizi, Sepideh Kavousi, Mohsen Asle Zaeem*

Department of Mechanical Engineering, Colorado School of Mines, Golden, CO 80401, USA

ARTICLE INFO

Article history:
Received 9 May 2021
Revised 8 February 2022
Accepted 18 March 2022
Available online 22 March 2022

Keywords:
Al-Cu alloys
Solidification pattern
Interfacial energy anisotropy
Molecular dynamics
Multi-phase field modeling

ABSTRACT

Combined effects of the cooling rate, alloy composition, and crystal-melt (CM) interfacial anisotropy on solidification of Al-Cu alloys are studied by integrating molecular dynamics and phase-field simulations. Capillary fluctuation method is used to determine the CM interfacial energy properties by molecular dynamics simulations for alloys ranging from 3 to 11 at% Cu. While the average CM interfacial energy decreases with increasing Cu content, its anisotropy does not present a clear trend with composition change. Primary and secondary dendrite arm spacings as well as θ-phase fraction are calculated by phase-field simulations, and validated against experimental measurements and analytical solutions at cooling rates ranging from 1 to 1250 K/s. Results show that the θ-phase fraction decreases with increasing the cooling rate, and this reduction is more drastic in alloys with a higher Cu content. Also, the microstructure features are influenced by the growth dynamics, where seaweed structure formation results in a more homogenous distribution of θ-phase and a finer microstructure. The effects of temperature gradient, Cu concentration gradient, and interfacial energy properties on the dendritic growth morphology of Al-Cu alloys are summarized by a map of supercooling versus the CM interfacial anisotropy to predict pattern formation. The results show that, irrespective of Cu content and cooling rate, the seaweed structure formation is halted at CM interfacial anisotropies larger than 0.005. As the anisotropy decreases, different seaweed structures can form regarding the constitutional supercooling. At low anisotropies (Al-3 and Al-8.4 at% Cu) and low supercooling (Al-3 at% Cu) fractal or degenerate seaweed is dominant while at high supercooling (Al-8.4 at% Cu) compact seaweed forms. This difference in supercooling stems from different solute atom transport rates.

1. Introduction

The crystal-melt (CM) interfacial energy is an intrinsic material property that plays a critical role in solidification pattern formation [1]. It influences the solidification microstructures in two ways; first, dendrites grow during solidification along the directions with the highest CM interfacial energy, and second, the instability of interface affecting the dendrite patterns, is controlled by the CM interfacial energy [2–4]. The CM interface energy has an anisotropic nature with respect to the crystallographic directions. Despite the unknown atomistic origin of interfacial energy anisotropy, the anisotropy is very small for most alloys which results in a negligible change in the interfacial energy in different crystallographic directions [1]. However, it governs the nucleation and growth kinetics [5–7], morphology [8–10], and crystallographic growth direction of the dendrites [11].

The instability of CM interface, which is influenced by the CM interfacial energy, controls microstructure evolution, dendrite arm spacing, and microsegregation patterns [3]. Coriell and Sekerka [12] added surface tension and surface kinetic anisotropy effects into the perturbation linear stability analysis and showed that the capillary term, that contributes in interface stability, is direction dependent [9,13,14]. Trivedi [15] compared experimental results with linear and weakly nonlinear analyses of the planar interface stability and showed that when a material is directionally solidified beyond the threshold of planar stability condition [16], the anisotropy of interface properties not only affects the planar to cellular and cellular to dendritic transitions, but also causes tilting of cells and dendrites against the heat flow direction [17–19].

Besides dendritic microstructures, diverse types of morphologies can be formed during solidification of metallic alloys, including seaweed, dense-branched, fractal-like, and variations between these patterns [20–24]. These morphologies may result from in-

* Corresponding author.
E-mail address: zaeem@mines.edu (M. Asle Zaeem).

https://doi.org/10.1016/j.actamat.2022.117859

teractive effects of thermal diffusion, mass diffusion, and inherent interfacial anisotropy on interface stability [22,25,26]. Experimental work performed by Akamatsu et al. on transparent alloys [22,26] showed that the stability of dendritic patterns greatly depends on the strength of interfacial energy anisotropy. They proved that for crystal orientations corresponding to low interfacial anisotropy, dendritic pattern is unstable and seaweed structure forms. Numerical studies [21,27] confirmed these results and proved sidebranching takes place for vanishing anisotropy which results in seaweed structure formation. Recent phase-field simulations show occurrence of transitions between solidification patterns by changing the chemical compositions and processing conditions [28–30]. Amoorezaei et al. [31] showed that in a directionally solidified Mg alloy with low interfacial energy anisotropy, any change in processing condition considerably alters the solidification morphology. Their results indicated that at a low pulling velocity, seaweed structure is dominant, while at an increasing pulling velocity compacted seaweed is the main morphology. In another study, Xing et al. [32] investigated the dynamics of growing dendrites and showed that the seaweed is the dominant morphology at weaker interfacial energy anisotropies, lower pulling velocities, and higher thermal gradients. It is believed that the instability at the tips, which stems from low surface energy anisotropy, is responsible for the formation of such a morphology [33,34]. Chen et al. [35] showed that tip splitting takes place during the solidification of Al-4 wt% Cu with low interfacial energy anisotropy, which leads to seaweed structure. They argued that the seaweed regime is formed by morphological instability occurring when the cell/dendrite tip becomes too wide.

Despite their importance in predicting the microstructure, experimental measurements of the CM interfacial free energy and the anisotropy terms are very challenging and often not possible [36]. Because of the recent availability of reliable embedded interatomic potentials for metals, molecular dynamics (MD) has become a popular method for calculating the CM interface free energy. Among the two well-known methods, namely Cleavage [37] and the capillary fluctuation method (CFM) [38], the latter results in a more accurate anisotropy parameter calculations, which is used in this study. CFM has been extensively used for interface energy calculations of metals [39–44], compounds [45], and binary alloys [46,47].

The interface energy for an alloy depends on the working temperature and alloy composition. There are different MD simulations that discuss how the change in chemical composition alters the interface free energy and its anisotropy. Becker et al. [48] used CFM to show that the CM interface energy in Ni-5at%Cu alloy is 7.4% less than pure Ni. Furthermore, the addition of 5 at% Cu decreases δ_1 (Fourfold anisotropy parameter) from 0.09 to 0.072 and increases δ_2 (Six-fold anisotropy parameter) from -0.011 to -0.007 [49]. Potter and Hoyt [50] applied the CFM to the Cu-rich Cu–Ag–Au system; they indicated that species with a high enthalpy of mixing tend to destabilize the dendrites growing in the ⟨100⟩ direction and promote a transition to the growth of hyper-branched and ⟨110⟩ –oriented dendrites. Kavousi et al. performed integerated MD and phase-field modeling of solidification highlighting how the working temperature affects the competition between solidification kinetics and capillary anisotropy on the pattern selection [28].

Some studies support the computationally-predicted change in the interface free energy and the corresponding anisotropy due to the change in alloy composition. Using experimental observation [51] and phase-field modeling [52], it was shown that in Al-Zn alloys (Zn <25 wt%) with high values of ϵ_1 (four-fold anisotropy parameter) and low values of $|\epsilon_2|$ (six-fold anisotropy parameter), ⟨100⟩ -oriented dendrites are dominant. When Zn concentration is more than 55 wt%, the value of ϵ_1 is low and the absolute value of ϵ_2 is high. Under this condition, ⟨110⟩ is found to be the favorable growth direction. In the intermediate regions, surface energy anisotropy becomes very small and leads to the formation of seaweed structures or hyper-branched dendrites [53]. The same behavior was observed in Al-Ge system, where at Ge less than 20 wt% dendrite grows along ⟨100⟩ direction, and when Ge is more than 46 wt%, ⟨110⟩ is dominant growth direction [54]. Recently, Wang et al. [1] showed that in Al-Sm alloy system, increasing Sm content drastically reduces anisotropy strength while increasing the average interface energy (γ_0). The aforementioned studies indicate that chemical composition is the main factor that controls CM interfacial energy and its anisotropy. Also, it was shown that since the equilibrium composition at CM interface changes by temperature, its energy and anisotropy are functions of temperature [55–57].

While the impact of CM interfacial anisotropy on the orientation selection and the interface stability is well established, there is a gap in the literature regarding its influence on the final phase fractions, arm spacing, and microsegregation. Furthermore, the combined effects of the CM interfacial anisotropy and alloying element content on growth dynamics are not well-understood. In this work, we performed an atomistic-informed phase-field study to investigate the microstructure evolution during solidification of Al-Cu binary alloys under different solidification conditions. First, MD simulations are performed to reveal the relationship between CM interfacial energy properties and Cu content. Subsequently, a multi-phase field model is utilized to explore how Cu concentration gradient ahead of growing dendrite (G_c) and CM interfacial anisotropy collaborate to generate different solidification patterns and consequently different solidification features, such as dendrite arm spacings, and θ-phase fraction and distribution. The simulation results are validated by comparison to experimental measurements and analytical solutions in a wide range of cooling rates from 1 to 1250 K/s.

2. Computational models and simulation procedures

We use multi-phase field modeling to study microstructure evolution and pattern formation during solidification of different compositions of Al-Cu binary system. MD simulations were completed to determine the CM interface energy and its anisotropy for different compositions.

2.1. Molecular dynamic simulations

In CFM [38], the interface stiffness is obtained based on the interface's fluctuation amplitude, cross-section, and target temperature. Fig. 1(a) demonstrates a snapshot of the simulation system. The simulation system contains the coexistence of solid-and liquid, where the central part is in the liquid phase, and the CM interface normal is considered parallel to the z-direction. The interface is quasi-two dimensional (2D), where the interface width along y-direction, b, is much shorter than its length along x-direction, W. The simulation size along z-direction is considered very large to avoid any interactions between the interfaces. The position of atoms located at the CM interface, as represented by orange color in Fig. 1(a), is used to determine the position of interface, $p(x)$, for each time frame. The deviation of the interface position from its mean value, $\langle p\rangle$, can be written as a summation of Fourier Modes, $p(x) - \langle p\rangle = \sum_k A(k)e^{ikx}$. Based on the equipartition of energy and considering the Fourier modes as the degrees of freedom, Eq. (1) relates the interface stiffness to the amplitudes and modes of Fourier transform.

$$\gamma + d^2\gamma/d\theta^2 = \frac{k_B T}{bW\langle|A(k)|^2\rangle k^2} \tag{1}$$

where k_B, is Boltzmann constant, T is the temperature, $\langle|A(k)|^2\rangle$ is the mean squared amplitude of the Fourier modes, and k is

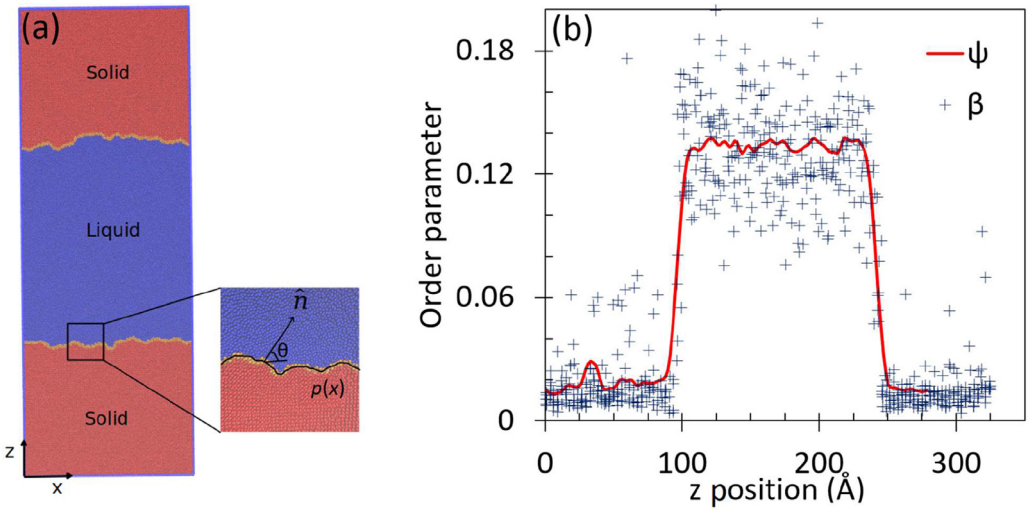

Fig. 1. (a) Snapshot of MD simulation system demonstrating the two-phase coexistence slab. The red and blue colors represent the solid and liquid phases, respectively. The atoms located at the interface are colored as orange. (b) Order parameters, ψ and β, as a function of z. They are used to identify the solid and liquid phases.

the mode wave number. γ is the CM interface free energy and $\gamma + d^2\gamma/d\theta^2$ is the interface stiffness, where θ is the angle between instantaneous local interface normal and the average orientation of interface. Interface free energy is an anisotropic property, and one can calculate the anisotropy term by considering different crystallographic orientations for the CM interface in the CFM. The spherical harmonic expansion of interface energy, which depends on interface normal orientation ($\hat{n}$), is represented:

$$\gamma\left(\hat{n}\right) = \gamma_0\left[1 + \delta_1\left(4\sum_{i=1}^{3} n_i^4 - 3\right) + \delta_2\left(\sum_{i=1}^{3} n_i^6 + 30n_1^2n_2^2n_3^2\right)\right], \tag{2}$$

where $n_i (i = 1, 2, 3)$ are the components of normal to the interface vector, $\hat{n}$ in x and y and z-directions, γ_0 is the mean CM interface free energy, and δ_1 and δ_2 are the anisotropy parameters, [58]. γ_0, δ_1, and δ_2 can be estimated by fitting the stiffness calculated from MD simulations to the analytical stiffness expression calculated from Eq. (2). Details on obtaining the analytical stiffness expressions for each orientation can be found in our previous works [41–44,46,47].

All the MD simulations are performed using LAMMPS (Large-scale Atomic/Molecular Massively Parallel Simulator) [59], and the Al-Cu interatomic potential used in this study is developed by Mahata and Asle Zaeem [47,60], which is based on the second nearest neighbor modified embedded atom method (2NN-MEAM). This potential is specifically developed to reproduce the high temperature thermophysical and transport properties of the binary Al-Cu system. It should be mentioned that we have recently performed an in-depth nanoscale solidification study of metals and performed uncertainty calculations to show the accuracy of MD simulations with 2NN-MEAM potentials [61,62].

Since fluctuations of CM interface must be performed on the fully equilibrated coexistence of CM, the equilibrium CM phase boundary compositions for different temperatures are required. Thus, the first step is performing MD simulations to calculate the phase diagram. The details of phase-diagram calculations are explained in our previous work [46]. We calculate the phase diagram for temperatures ranging between 925 K (melting point of pure Al) and 860 K.

For [100]-oriented CM interface, first the interface energy is calculated by MD simulations using 50 × 4 × 80 face-centered cubic (fcc) unit cells (6400 atoms) of pure Al with [001] orientation along the z-direction. The simulation systems with [110] and [111] interface orientations have similar dimensions and number of atoms. First, the simulation system is equilibrated under NPT ensemble at the target temperature for 100 ps. Then, the central half of the system is melted by performing an NVT ensemble, at $T = 2000$ K, for 40 ps, while keeping the rest of system unchanged. The temperature of the system is reduced to the target temperature, and to determine the interface energy of Al-Cu systems, some of the Al atoms in the solid and liquid phases are replaced by Cu alloys such that the final solute concentration in each phase is consistent with the phase diagram. The simulation box sizes in the x and y-directions are adjusted to obtain the correct lattice parameter of the solid phase at the target temperature and composition. This lattice parameter is obtained from a separate MD simulation on a system having solute concentration corresponding to the target temperature.

After proper size scaling of the simulation box, the system is equilibrated under a hybrid $NP_{ZZ}T$ (isothermal-isobaric) MD/Monte Carlo (MC) ensemble. During this process, the box size is only allowed to change in the z-direction, and the equilibration of concentration is performed using MC to randomly attempt swapping 3000 Al and Cu atoms every 5000 steps. The overall equilibration time considered ranges between 1 and 2 ns. During this process, the potential energy of the system should approximately stay constant during the last 200 ps of the equilibration time. At the final step, an NPH ensemble (isoenthalpic–isobaric) is performed for 240 ps. During this step, the system configuration is saved every 1 ps for further analysis of the interface fluctuations.

Further analysis of the trajectory files is required to determine the local interface position, $p(x)$. This is performed by introducing an order parameter, β, for each atom, which identifies the solid and liquid phases by comparing the positions of its 12 first neighbors with their perfect crystal, $\vec{r}_{FCC}$ [40].

$$\beta = \frac{1}{12}\sum_i |\vec{r}_i - \vec{r}_{FCC}|^2 \tag{3}$$

This order parameter fluctuates a lot, as presented in Fig. 1(b), which makes the determination of interface position challenging. Thus, a new order parameter, ψ, was introduced by Asadi et al. which uses a smoothing function, w_d, to reduce fluctuations of β [42]:

$$\psi(x, z) = \frac{\sum_i w_d r_i \beta_i}{\sum_i w_d r_i}, \tag{4}$$

where $w_d = [1-(r_i/d)^2]^2$, $r_i = \sqrt{(x_i-x)^2+(z_i-z)^2}$. The smoothing is performed over cylinders perpendicular to the y-direction with the radius of d. Fig. 1(b) shows the change of ψ and β along the z-direction. The initial order parameter, β, fluctuates a lot, therefore the smoothened order parameter, ψ, is used, which approximately takes constant values in solid and liquid, and the location of the interface is defined to be where ψ is halfway between those values. By performing Fourier transform on the interface position data and averaging the Fourier amplitude over all the time frames, we use Eq. (1) to calculate the interface stiffness. Details on calculating concentration variations across the interface can be found in [63].

2.2. Multi-phase field modeling

In this paper, a multicomponent multiphase-field model presented by Eiken et al. [64] is used, which is implemented in the software MICRESS® (version 6.4) [65]. Three non-conserved order parameters were assigned for liquid, α-phase (fcc-Al) and Al_2Cu, and one conserved order parameter, c, was assigned for Cu concentration. The phase-field equation governing the interface kinetics is expressed as [66],

$$\dot{\varphi}_\alpha = \sum_{\beta\neq\alpha}^{\nu} \mathrm{M}^{\varphi}_{\alpha\beta}\left[\mathrm{b}\Delta\mathrm{G}_{\alpha\beta} - \sigma_{\alpha\beta}\left(\mathrm{K}_{\alpha\beta}+\mathrm{A}_{\alpha\beta}\right) + \sum_{\gamma\neq\beta\neq\alpha}^{\vartheta}\mathrm{J}_{\alpha\beta\gamma}\right]. \tag{5}$$

$\dot{\varphi}_\alpha$ is the time derivative of order parameter, where, α, β, and γ represent three different phases, and ν is the number of grains in the system. The subscripts $\alpha\beta$ and $\alpha\beta\gamma$ represent the interface between grains with α and β phases, and the triple point junction between grains with α, β, and γ phases, respectively. Parameter $\mathrm{M}^{\varphi}_{\alpha\beta}$ represents the phase-field mobility of the interface $\alpha\beta$ and is related to the kinetic coefficient in the Gibbs-Thomson equation, $\mu^{\mathrm{G}}_{\alpha\beta}$ (also known as the sharp interface mobility), through Eq. (6) [66].

$$\mathrm{M}^{\varphi}_{\alpha\beta} = \frac{\mu^{\mathrm{G}}_{\alpha\beta}}{1+\frac{\mu^{\mathrm{G}}_{\alpha\beta}\eta\Delta s_{\alpha\beta}}{8}\left\{\sum_{\mathrm{i}}\mathrm{m}^{\mathrm{l}}_{\mathrm{i}}\sum_{\mathrm{j}}\left[\left(\mathrm{D}^{\mathrm{ij}}_{\alpha}\right)^{-1}\left(1-\mathrm{k}_{\mathrm{j}}\right)c_{j\alpha}\right]\right\}}. \tag{6}$$

η is the interface thickness in the phase-field simulations, $\Delta s_{\alpha\beta}$ is the entropy change during α to β phase transformation, $\mathrm{m}^{\mathrm{l}}_{\mathrm{i}}$ is the slope of the liquidus line, $\mathrm{D}^{\mathrm{ij}}_{\alpha}$ is the diffusion matrix in α phase, and k_{j} is the partition coefficient of solute atom j. For alloys where η is finite, the equation will result in a phase-field mobility that is smaller than the sharp interface mobility.

The first ($\mathrm{b}\Delta\mathrm{G}_{\alpha\beta}$), second ($\sigma_{\alpha\beta}(\mathrm{K}_{\alpha\beta}+\mathrm{A}_{\alpha\beta})$), and third ($\sum_{\gamma\neq\beta\neq\alpha}^{\vartheta}\mathrm{J}_{\alpha\beta\gamma}$) terms on the right-hand-side of Eq. (5) represent the bulk, interface, and high order junction energy terms, respectively. In the first term, b is the pre-factor and $\Delta\mathrm{G}_{\alpha\beta}$ is the molar Gibbs free energy density calculated by Eqs. (7) and (8), respectively.

$$b = \frac{\pi}{\eta}\left(\varphi_\alpha+\varphi_\beta\right)\sqrt{\varphi_\alpha\varphi_\beta}\,. \tag{7}$$

$$\Delta\mathrm{G}_{\alpha\beta} = \frac{1}{\mathrm{v}^{\mathrm{m}}}\left[\mu^{\mathrm{i}}_{\beta}\left(\vec{c}_\beta\right)-\mu^{\mathrm{i}}_{\alpha}\left(\vec{c}_\alpha\right)\right]. \tag{8}$$

v^{m} is the molar volume of the phases, $\vec{c}_\alpha$ and $\vec{c}_\beta$ are concentration of solvent in α and β phases, $\mu^{\mathrm{i}}_{\beta}(\vec{c}_\beta)$ and $\mu^{\mathrm{i}}_{\alpha}(\vec{c}_\alpha)$ are the chemical potential of component i in α and β phases, which are defined as the increment in the Gibbs free energy of the phases, G_α or G_β, when a very small moles of species i, n^i, is added to these phases, while all other variables of the phase are kept constant.

In the second term of Eq. (5), $\sigma_{\alpha\beta}$, $\mathrm{K}_{\alpha\beta}$, and $\mathrm{A}_{\alpha\beta}$ represent the interfacial energy, pairwise curvature, and anisotropy of the interface $\alpha\beta$, respectively. While $\sigma_{\alpha\beta}$ is a constant value, $\mathrm{K}_{\alpha\beta}$ is calculated by

$$K_{\alpha\beta} = \frac{\pi^2}{2\eta^2}\left(\varphi_\beta-\varphi_\alpha\right)+\frac{1}{2}\left(\nabla^2\varphi_\beta-\nabla^2\varphi_\alpha\right). \tag{9}$$

And the anisotropy of the interface for cubic symmetry is given by

$$\mathrm{A}_{\alpha\beta} = 1+\varepsilon_4\cos(4\varphi). \tag{10}$$

ε_4 is the strength of anisotropy, $\varepsilon_4 \in (0\ 1)$, and φ is the azimuthal angle measured from a reference direction.

The high order triple junction term in the third term of Eq. (5), $\mathrm{J}_{\alpha\beta\gamma}$, is calculated from Eq. (11) as

$$\mathrm{J}_{\alpha\beta\gamma} = \frac{1}{2}\left(\sigma_{\beta\gamma}-\sigma_{\alpha\gamma}\right)\left(\frac{\pi^2}{\eta^2}\varphi_\gamma+\nabla^2\varphi_\gamma\right). \tag{11}$$

Solute diffusion is described by [66]:

$$\dot{c}^i = \nabla\sum_{\alpha=1}^{\nu}\sum_{j=1}^{n-1}\varphi_\alpha\mathrm{D}^{\mathrm{ij}}_{\alpha}\nabla c^j_\alpha. \tag{12}$$

For a system with n species, $c^{i=1.....n-1}$ are the concentrations of the solute species. Diffusion coefficients D^{ij}_{α} are functions of temperature individually for each phase in an Arrhenius approach. The simulations started from 100% liquid phase at liquidus temperatures. The liquidus temperatures for Al-Cu alloys with 3, 6, 8.4 and 10.6 at% Cu were obtained from Thermo-Calc simulations, and they are 915.35 K, 897.8 K, 883.13 K, and 869.3 K, respectively. Heat is extracted from the bottom boundary into an external medium with a fixed temperature of 298 K and different heat transfer coefficients (h) of 0.5, 2, and 4 W/cm^{2}K. Two sets of phase-field simulations are performed in this study. The first set is for validating the dendrite arm spacing with experimental measurements, and it is executed in a 2D domain of 600 μm × 1000 μm with grid spacing of $\Delta x = \Delta y = 100$ nm. Also, a 3D simulation on a domain of 150 μm × 150 μm × 150 μm with the same grid spacing was performed; it should be mentioned that in the validation section, all heat transfer coefficients are less than 0.5 W/cm^{2}K. The second set of simulations (parametric study) were executed on a 2D domain of 150 μm × 150 μm with a grid spacing of 100 nm for $h = 0.5$ W/cm^{2}K and grid spacing of 50 nm for $h = 2$ and $h = 4$ W/cm^{2}K. We used an embedded model for heterogeneous nucleation that creates randomly oriented initial seeds of the solid phase α at the bottom boundary (with 1 μm thickness) whenever the local supercooling exceeds the required critical value (1 K for all simulations), while further nucleation is prohibited. Al_2Cu nucleation takes place at the interfaces of α/liquid with the same supercooling criterion [67]. The interaction between Al_2Cu with liquid and alpha phases was considered to be isotropic. The interfacial energies of Al_2Cu/liquid and Al_2Cu/alpha were set at 9.2×10^{-6} J/cm^2 [68] and 3.7×10^{-5} J/cm^2 [69], respectively.

The set of multi-phase-field equations are solved using finite-difference method to simulate the growth of the phases [70]. Solute redistribution is evaluated at all phase interfaces under the constraint of equal diffusion potentials [64]. Diffusion of Cu is solved in the liquid and α-phase under consideration of a numerical anti-trapping current within the diffuse interface regions [71]. Temperature is evaluated in the direction of heat flow (1-D temperature field). The conductivities of liquid and α-phase are set to 1.5 and 1.9 W/cm.K, respectively [72–74]. All thermodynamic material properties such as driving forces, local supercooling, interface concentrations, heat capacity, enthalpy, and latent heat as well as the diffusion kinetics required for the phase-field simulation are calculated using Thermo-Calc and are passed to MICRESS through

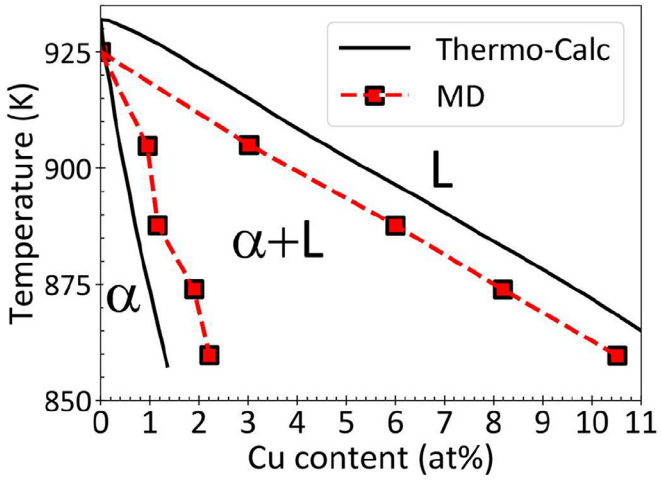

Fig. 2. Al-rich composition-temperature phase diagram for Al-Cu alloy calculated by MD simulations and Thermo-Calc. The symbols L and α denote the liquid and solid (α-Al) phases, respectively.

Table 1
The expressions of interface free energy, γ, and stiffness, $\gamma + d^2\gamma/d\theta^2$, for various interface orientations, as given by Eq. (2).

orientation	γ	$\gamma + d^2\gamma/d\theta^2$
100 [001]	$\gamma_0\,[1 + \delta_1 + \delta_2]$	$\gamma_0\,[1 - 15\,\delta_1 - 5\,\delta_2]$
001 [110]	$\gamma_0\,[1 - \delta_1 + 0.25\,\delta_2]$	$\gamma_0\,[1 - 9\,\delta_1 + 13.75\,\delta_2]$
$1\bar{1}0$ [110]	$\gamma_0\,[1 - \delta_1 + 0.25\,\delta_2]$	$\gamma_0\,[1 + 15\,\delta_1 + 6.25\,\delta_2]$
$1\bar{1}0$ [111]	$\gamma_0\,[1 - 1.67\,\delta_1 + 1.22\,\delta_2]$	$\gamma_0\,[1 + 9\,\delta_1 - 9.45\delta_2]$

the TQ-interface (Thermodynamic Calculation Interface). The thermodynamic and mobility databases used for the current study are TCAL7 (Thermo-Calc database for Al-based alloy, version 7) and MOBAL5 (Al-based alloy mobility database, version 5).

Boundary conditions for phase-field order parameters and concentration are periodic at the left and right boundaries of the 2D domain, and the Neumann boundary condition (no-flux) is applied at the top and bottom boundaries. Boundary conditions for temperature are as follows: fixed at the bottom and the Neumann boundary condition (no-flux) at the top, left, and right boundaries.

3. Results and discussion

Al-Cu alloys with 3, 6, 8.4, and 10.6 at% Cu are studied in this work. Solidification takes place by removing heat from the bottom surface of the 2D domains under different heat transfer coefficients of 0.5, 2, and 4 W/cm^{2}K. First, the effect of Cu content on CM interfacial energy and its anisotropy is investigated through MD simulations. Then, multi-phase modeling is used to study microstructure evolution and solidification pattern formation in the aforementioned Al-Cu alloys.

3.1. Crystal-melt interfacial free energy and related anisotropy calculations

The first step for calculating CM interfacial free energy is obtaining the equilibrium crystal-melt phase boundary compositions for different temperatures. Interface energy calculations are performed on systems with Cu compositions ranging between 3 and 11 at%; the corresponding portion of the Al-Cu phase diagram, calculated by MD simulations and Thermo-Calc, is presented in Fig. 2.

MD simulations are performed considering different orientations for the interface normal and interface width, given by [] and $\langle\,\rangle$, respectively. Table 1 summarizes the details of the investigated orientations and the corresponding interface energy and stiffness

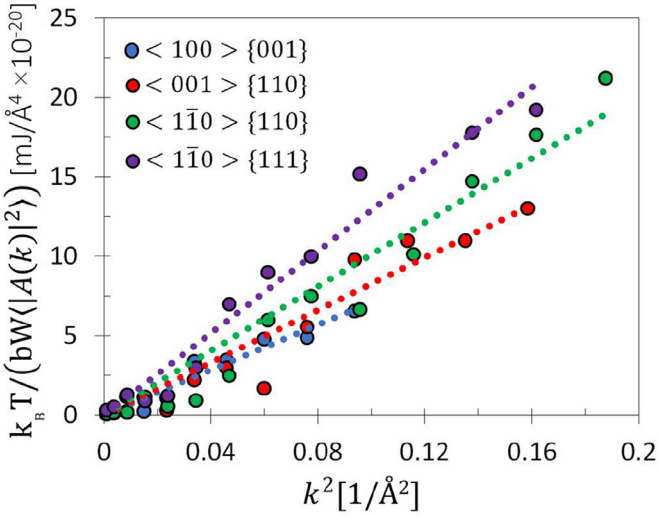

Fig. 3. The variation of $k_BT/(bW\langle|A(k)|^2\rangle)$ versus k^2 for different orientations as obtained by MD simulations of Al-Cu binary system at $T = 888$ K with solidus and liquidus Cu compositions equal to 1.16 and 6 at.%. The dotted lines are linear fits to symbols with the same color.

expressions using Eq. (2). For interface planes with three-fold or higher symmetry, the stiffness value does not depend on the orientations in which the interface is curved [75]. [110] oriented interface is an example that includes a two-fold symmetry. Thus, as demonstrated in Table 1, considering two different orientations ($\langle 001\rangle$ and $\langle 001\rangle$) in the x-direction alters both the stiffness expression and its value. For the [110] CM interface, we performed two separate simulations, and one can distinguish the difference in their stiffness expressions presented in Table 1.

For each orientation, the interface stiffness is estimated by the slope of line fitting $k_BT/(bW\langle|A(k)|^2\rangle)$ versus k^2. The stiffness values calculated by MD simulations are fitted to the stiffness expressions using Eq. (2) to calculate the average CM interface free energy and the anisotropy parameters. Fig. 3 shows the variation of $k_BT/bW < |A(k)|^2 >$ versus k^2 for the CM interface energy of the Al-Cu binary system at $T = 888$ K with the solidus and liquidus Cu compositions equal to 1.16 and 6 at%.

It should be mentioned that Eq. (1) fails for small wavelengths, and a logarithmic behavior is expected for large values of k [49]. Thus, in the fitting process and stiffness calculations, only the portion of the MD results related to the linear section is used in the analysis. The fitting process results in $\gamma_0 = 96.11 \pm 7.4$ mJ/m^2, $\delta_1 = 0.014$, and $\delta_2 = -0.0042$. Considering $\delta_1 > 0$ and a small value for δ_2, Eq. (2) produces either [100] and [110] dendrites. Larger δ_1 results in the growth of [100]-oriented dendrites, but when $\delta_2 < 0$, [110] dendrites can also grow [52]. A similar process is repeated for all the other binary systems. The interface energy and anisotropy parameters are summarized in Table 2.

Each binary system is represented by a temperature and the corresponding equilibrium liquidus and solidus concentrations. The results do not reveal a trend line for the anisotropy changes, but the mean CM interface free energy decreases by a decrease of temperature (an increase in solute concentration). In 2D, the interfacial energy is:

$$\gamma = \gamma_0(1 + \varepsilon_4(\cos 4\varphi)), \tag{13}$$

where ε_4 is the anisotropy parameter in 2D, and φ is the azimuthal angle. Using trigonometric relations, ε_4 is calculated as a function of 3D anisotropy parameters (δ_1 and δ_2) and presented in Table 2. It was noted that ε_4 obtained for alloys with $C_s = 0.96$ and 1.93 at% are much smaller than 0.01 which is a common anisotropy used

Table 2
The average interface free energy, γ_0 (mJ/m^2), anisotropy parameters, δ_1 and δ_2, defined in Eq. (2), and ε_4, defined in Eq. (13), for four Al-Cu binary systems. Each binary system is identified by the solidus, C_S, and liquidus, C_L, compositions at temperature T, which are obtained from the phase diagram, Fig. 2.

	γ_0	δ_1	δ_2	ε_4
Case I: T = 905 K C_s = 0.96 at% C_L = 3.05 at%	110 ± 4.9	0.0045	−0.0026	0.0035
Case II: T = 888 K C_s = 1.16 at% C_L = 6.0 at%	96.11 ± 7.4	0.014	−0.0042	0.0124
Case III: T = 874 K C_s = 1.93 at% C_L = 8.2 at%	92.24 ± 7.3	0.008	−0.0044	0.0050
Case IV: T = 860 K C_s = 2.2 at% C_L = 10.6 at%	89.8 ± 6.9	0.01	−0.0079	0.0071

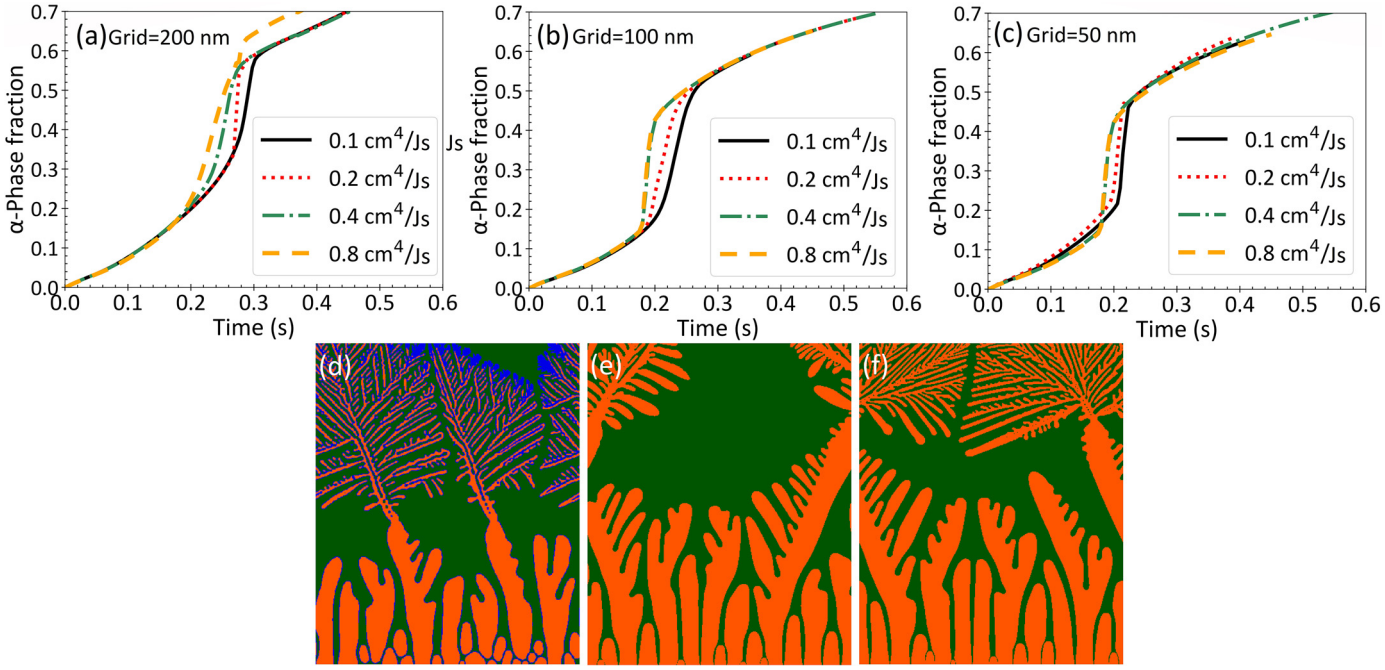

Fig. 4. Grid convergence data (a–c) α-Phase fraction as a function of time with different grid sizes and IM values at heat transfer coefficient of h = 0.5 W/cm^{2}K, (d–f) related microstructure at IM of 0.8 cm^4/Js and different grid size, (d) 200 nm, (e) 100 nm, and (f) 50 nm; orange and green colors show solid and liquid phases, respectively. Numerical instability takes place when the grid size is 200 nm while no instability was observed when grid size is set to 100 and 50 nm, even for very high IM values.

for FCC alloys in literature. Details of ε_4 calculations are presented in Appendix 1.

3.2. Grid convergence study

Grid convergence study was conducted for directional solidification of Al-3 at% Cu with different heat transfer coefficients (h), to demonstrate that the solution is independent of the discretization at different growth rates. Grid spacing is not the only numerical parameter that influences simulation results, and proper interface mobility (IM) values need to be determined to guarantee diffusion-controlled growth without kinetically slowing down the interface [65]. In order to determine the appropriate grid size and IM, simulations should be run with different IM values for a constant grid size, and phase fraction versus time should be plotted for quantitative grid resolution study [65]. Two behaviors can be noticed when increasing the IM value. For large grid sizes, the growth rate increases as we raise IM, resulting in numerical instability of the results. When the grid spacing is fine enough, however, the growth rate will attain a constant value as we raise IM and will remain constant even at higher IM levels. In this study, heat transfer coefficients were set to h = 0.5, h = 2, and h = 4 W/cm^{2}K, and for each heat transfer coefficient, a grid resolution study was conducted where domain size was 100 μm by 120 μm. Fig. 4(a)–(c) show α-phase fraction as a function of time for grid size of 200, 100, and 50 nm at different IM values for h = 0.5 W/cm^{2}K. It is clear that for all grid sizes, the growth rate of α-phase increases by increasing IM. While for grid spacing of 200 nm, numerical instability takes place at IM of 0.8 cm^4/Js and no instability was observed in the case of grid sizes of 100 and 50 nm. The solidification microstructure for different grid size at IM of 0.8 cm^4/Js are shown in Fig. 4(d)–(f). These results prove that by choosing a grid size of 100 nm and an IM value of 0.4 cm^4/Js when heat transfer coefficient is h = 0.5 W/cm^{2}K, the solution is independent of grid size. Furthermore, the minimum tip radius of the seaweed pattern at h = 0.5 W/cm^{2}K is 600 nm which is much higher than the selected grid size. It should be mentioned that MICRESS calculates the interface curvature directly by using the divergence of the interfacial normal vector. The interface curvature (k_{int}) over simulation time is used to calculate the tip minimum radius, $R_{tip} = 1/\kappa_{tip}$.

The same procedure was followed to perform grid convergence studies for heat transfer coefficients of 2 and 4 W/cm^{2}K. The results demonstrated that the results are independent of grid size for both heat transfer coefficients when the grid size and IM value are 50 nm and 0.4 cm^4/Js, respectively. The minimum tip radius of the seaweed pattern at h = 2 and 4 W/cm^{2}K is about 350 and 300 nm, respectively, which is much higher than the selected grid size.

3.3. Comparison of predicted primary dendrite arm spacing to experiments

Simulation results of the primary dendrite arm spacing (λ_1) of Al-3 at% Cu (Al-6.9 wt% Cu) are validated by experimental mea-

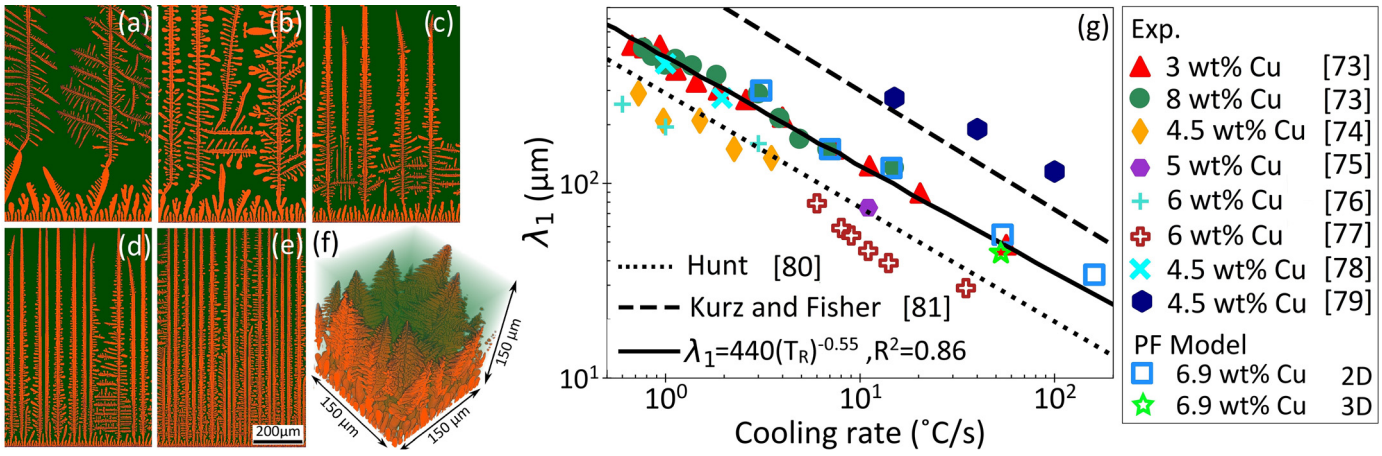

Fig. 5. Predicted microstructure using 2D phase-field simulations at different cooling rates (a) 3.2 °C/s, (b) 7 °C/s, (c) 17 °C/s, (d) 52 °C/s, and (e) 165 °C/s; (f) 3D phase-field simulation at cooling rate of 52 °C/s; orange and green colors show solid and liquid phases, respectively; and (g) comparison of the experimentally measured primary dendrite arm spacing with phase-field simulation results.

surements [76–82] and analytical solutions [83,84]. We performed 2D phase-field simulations of solidification for cooling rates ranging between 3.2 and 165 ℃/s. Also, a 3D phase-field simulation is completed to show there is only a negligible difference between 2D and 3D simulations in this study. Fig. 5(a–f) present the dendritic microstructure at different cooling rates, and the overall comparison of the phase-field results with the experimental measurements and analytical solutions is summarized in Fig. 5(g). The model predictions are in good agreement with the experimental measurements. Also, it is evident that at low cooling rates, long secondary arms are developed in directions that are not necessarily perpendicular to primary arms; while by increasing the cooling rate, secondary arms get shorter and are perpendicular to primary dendrites. This change of secondary arm features with cooling rate has been observed in both experimental [85] and simulation [86] studies. It should be noted that in the case of 3D simulation, the primary dendrite arm spacing was obtained using the Voronoi Warnken–Reed approach [87]. Nine dendrites are formed in the structure presented in Fig. 5(f). The traditional approach for measuring λ_1, is given by $\lambda_1 = c\sqrt{A/n}$, where n is the number of dendrites, A is the area normal to growth direction, and c is a coefficient set to 1.075 for hexagonal array of points in a 3D simulation [88]. This approach suggests $\lambda_1 = 53.75\ \mu$m which is very close to the obtained value from the 2D simulation with the same cooling rate (52 °C/s).

3.4. Microstructures characteristics

We investigate the microstructural features and how they are related to solidification conditions. The microstructures of solidified Al-Cu alloys with different heat transfer coefficients (different h) predicted by phase-field simulations are presented in Fig. 6. In this figure, green, white and red colors represent α-phase, θ-phase, and liquid, respectively. The solidified microstructures are different in many aspects, including primary and secondary arm spacing, phase fractions, and phase distribution. These diverse microstructures stem from different growth dynamics of dendrites during solidification, which are influenced by solute atom redistribution, the anisotropy of CM interface energy, and cooling conditions. We will focus on the solidification pattern formation in the following subsection (3.5), and here we focus on analyzing the microstructural features.

For all investigated alloys, when the heat transfer coefficient is 0.5 W/cm^{2}K, dendrites are tilted against the heat transfer direction (HTD). By increasing h to 2 and 4 W/cm^{2}K, they get aligned with HTD. In addition to the change in dendrite growth direction, dendritic morphologies in different alloys show different behaviors by increasing h, especially for Al-3 and Al-8.4 at% Cu. Due to low CM interfacial energy anisotropy, a morphology known as seaweed structure forms during solidification, with a morphology very sensitive to cooling conditions (discussed in Section 3.5). On the other hand, in alloys with 6 and 10.6 at% Cu dendritic morphology is dominant in all heat transfer coefficients.

In order to gain further insights into the effect of Cu content and cooling condition on the solidification microstructure of Al-Cu alloys, it is necessary to quantitatively show how microstructure characteristics change with these parameters. Fig. 7(a) and 7(b) compare simulations and analytical results of primary dendrite arm spacing (λ_1) and secondary dendrite arm spacing (λ_2) at different heat transfer coefficients.

A few analytical models have been proposed for predicting λ_1 [84,89–91] and all of them have a similar form to the model presented by Dantzig and Rappaz [3]:

$$\lambda_1 = \left(\frac{72\pi^2\Gamma_{sl}D_l\Delta T_0}{k_e}\right)^{\frac{1}{4}} (v^*)^{-\frac{1}{4}}\ (G)^{-\frac{1}{2}}\ . \tag{14}$$

Γ_{sl} is the Gibbs-Thomson coefficient, D_l is diffusion coefficient of solute atom in liquid, and ΔT_0 is freezing range. For the analytical solutions presented in Fig. 7, the material properties are obtained from MD and Thermo-Calc simulations. In addition, the processing conditions, namely the interface velocity (v^*) and the temperature gradient (G), are obtained from phase-field simulation results. The required data and the procedure for calculation of dendrite arm spacings via analytical solutions are represented in appendix 2.

In Fig. 7(a), λ_1 decreases as the heat transfer coefficient and Cu content increase. These results agree with the experimental measurements [76,92,93] and analytical solutions presented in Fig. 7(a). Furthermore, it can be seen from this figure that the effect of Cu content on λ_1 is more pronounced at a lower cooling rate (h = 0.5 W/cm^{2}K) and decreases with an increase in h. Based on Eq. (14), the parameters affecting λ_1 are divided into two main groups: material properties and processing conditions. Considering the data in Table A.2 (in the Appendix), for h = 0.5 W/cm^{2}K, the net effect of the processing condition ($(v^*)^{-\frac{1}{4}}\ (G)^{-\frac{1}{2}}$) considerably decreases with Cu content. But for other two h values, the decrease of $(v^*)^{-\frac{1}{4}}\ (G)^{-\frac{1}{2}}$ with the increase of Cu content is minor. In addition, material properties effect in Eq. (14) show a decreasing behavior by increasing Cu content. Both D_l and ΔT_0 decrease

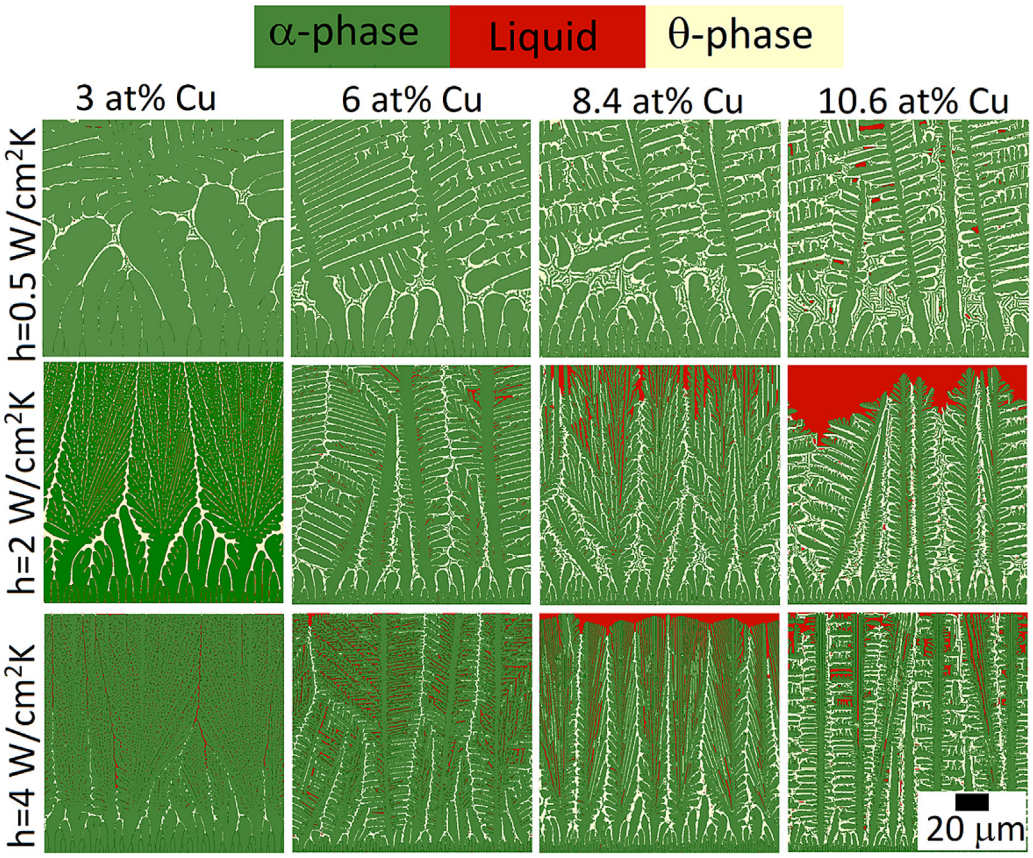

Fig. 6. Microstructures of Al-Cu alloys solidified with different heat transfer coefficients. For all the simulations, the snapshots are taken when the temperature of top surface reaches 397 K.

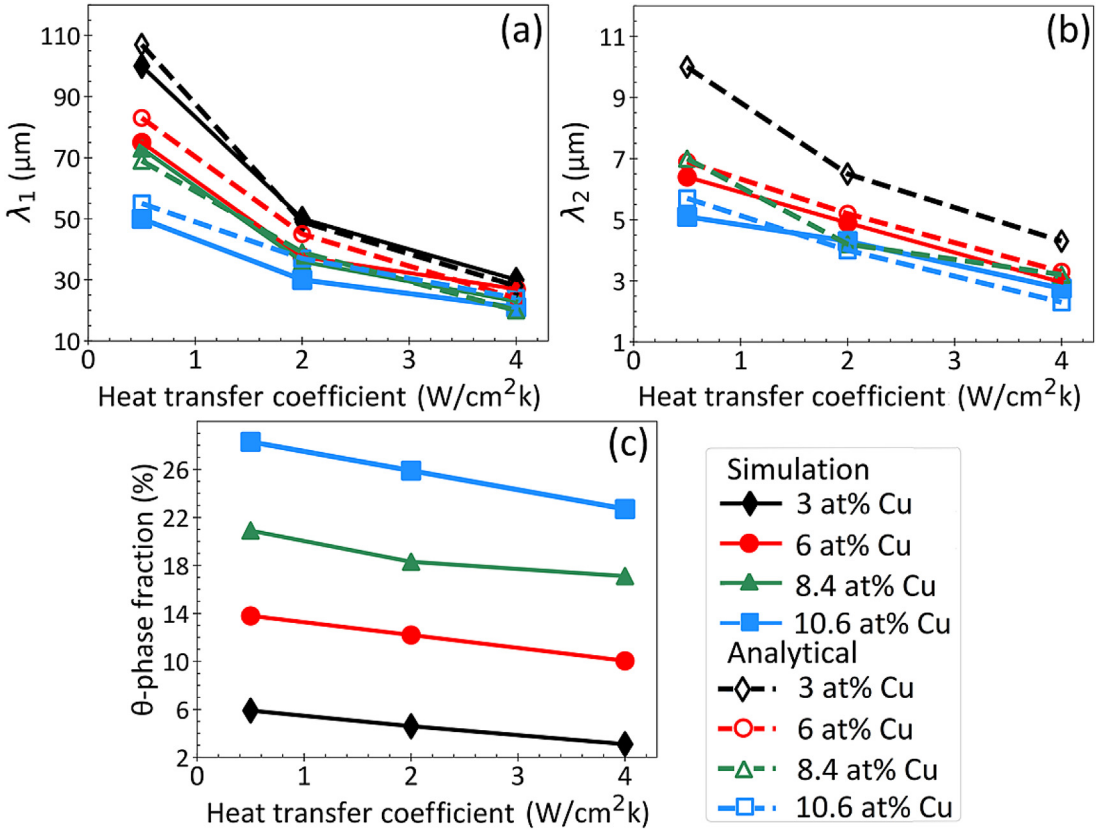

Fig. 7. Effect of heat transfer coefficient content on (a) λ_1, (b) λ_2, and (c) θ-phase fraction for different alloys.

with increasing Cu content [94] and their values are presented in Table A.1 (in the Appendix). Also, for a 2D simulation of a crystal with four-fold symmetry, the Gibbs-Thomson coefficient is given by [95]:

$$\Gamma_{sl} = \frac{\gamma_0(1 - 15\varepsilon_4(\cos 4\varphi))}{\rho \Delta s_f}, \quad (15)$$

where ρ is alloy density, and Δs_f is entropy of fusion. The value of Γ_{sl} for alloys with 3, 6, 8.4, and 10.6 at% Cu are 6.63×10^{-8}, 4.83×10^{-8}, 5.25×10^{-8}, and 5.16×10^{-8} Km, respectively. (presented in the Appendix). Overall, the decrease of D_l and ΔT_0, and the oscillating change of Γ_{sl} with the increase of Cu lead to decrease of λ_1 with Cu.

The analytical model for calculation of λ_2 was presented by Dantzig and Rappaz [3]:

$$\lambda_2 = 5.5\left(-\frac{\Gamma_{sl} D_l \ln\left(\frac{C_{eut}}{C_0}\right)}{m_l(1-k_e)(C_{eut}-C_0)}\right)^{\frac{1}{3}}\left(\frac{\Delta T_0}{Gv^*}\right)^{\frac{1}{3}}, \quad (16)$$

where C_{eut} is the final composition of liquid just before solidification, and m_l is the local temperature-concentration slope at the liquidus line of the given alloy, which are both extracted from Thermo-Calc simulation.

Fig. 7(b) shows that λ_2 decreases by increasing h and Cu content, but again the rate of change is higher with Cu at $h = 0.5$ W/cm^{2}K. In all cases, increasing Cu content decreases λ_2 indicating that finer microstructures are obtained at higher Cu contents, which is in agreement with experimental observations [92] and analytical models [3,96,97]. It should be noted that in case of alloys with 3 and 8.4 at% Cu, specially at high h values ($h = 2$ and $h = 4$ W/cm^{2}K), seaweed structure is dominant. In seaweed structures, measuring λ_2 is not as straight forward as in dendritic structures and it depends on the location and direction in which the distance between subbranches is measured. So, it is not possible to report a unique and consistent λ_2 for seaweed structures. Therefore, we do not report simulation results for secondary dendrite arm spacing in case of Al-3 and Al-8.4 at% Cu in Fig. 7(b), but analytical results related to these two alloys are presented.

Fig. 7(c) shows the effect of heat transfer coefficient on the θ-phase fraction (θ-PF) in the investigated alloys. The results show that by increasing h, the amount of θ-phase for all alloys decreases linearly. This behavior has been observed in experimental work too [92]. In all alloys, θ-phase forms via eutectic reaction but at different supercooling which is imposed by different heat transfer coefficients. Fig. 8 shows the phase fraction change as a function of time for different alloys and heat transfer coefficients. This figure indicates that in equilibrium conditions (obtained from Thermo-Calc) eutectic reactions take place at 820.75 K. When $h = 0.5$ W/cm^{2}K, eutectic reaction takes place at 819.4 K (1.3 K supercooling) in all alloys and results in the formation of a eutectic structure. In this condition, the amount of θ-phase is less than equilibrium for all alloys because more α-phase has formed before the nucleation of θ-phase. For example, in the case of Al- 6at% Cu, nucleation of θ-phase in equilibrium condition takes place when the amount of liquid is equal to 23% but at $h = 0.5$ W/cm^{2}K the amount of liquid is 21% before θ-phase nucleation. The eutectic structure is shown in Fig. 9 for Al-10.6 at% Cu, where it is obvious that $\theta+\alpha$ phases simultaneously grow within the liquid phase. The eutectic structure is not completely lamellar and consists of both lamellar and wavy structures, which were also observed in experimental studies [98,99]. The lamellar spacing is 1.2±0.2 μm for all alloys at $h = 0.5$ W/cm^{2}K.

By increasing h to 2 W/cm^{2}K, eutectic reaction starts at 813.6 K (7.15 K supercooling). In this situation, a higher amount of α-phase forms before nucleation of θ-phase and less liquid will transform into a $\alpha+\theta$ structure via eutectic reaction (18% liquid in the case of Al-6 at% Cu). Also, due to higher cooling rates, all Cu atoms cannot segregate from the α-phase into the interdendritic region and coring takes place [100,101], and consequently the amount of θ-phase decreases. In this condition, the lamellar spacing is 0.7 ± 0.1 μm for all alloys. By increasing h to 4 W/cm^{2}K, θ-phase starts to form at 803±4 K (17–21 K supercooling) through both eutectic reaction and direct solidification from enriched liquid. In this situation, the amount of liquid phase before eutectic reaction has decreased even more (14.5% in the case of Al-6 at% Cu) and coring is more severe, which results in a reduction of θ-phase.

In addition to the variation of θ-phase fraction with Cu content and heat transfer coefficient, its distribution also changes considerably with these parameters. It can be seen in Fig. 6 that at a constant heat transfer coefficient, θ-phase distribution is more homogenous in Al-3 and Al-8.4 at% Cu alloys than in Al-6 and Al-10.6 at% Cu. In the latter cases, dendritic morphology is dominant and θ-phase forms in interdendritic regions, while in the former cases, primary α-phase solidifies as a seaweed structure and θ-phase forms between seaweed branches. The underlying reasons for the different structures of α-phase during solidification have been discussed in the next section. In all investigated alloys by increasing heat transfer coefficient, the distribution of phase becomes more homogenous but this homogenization is more noticeable in alloys with 3 and 8.4 at% Cu. In these alloys, tip splitting frequency increases considerably as the heat transfer coefficient raises. As a consequence, the distribution of the θ-phase becomes more homogenous. By comparison of the two left columns in Fig. 6, it is completely obvious that θ-phase distribution is more homogenous in seaweed structures (Al-8.4 at% Cu) than in dendritic structures (Al-10.6 at% Cu), and θ-phase distribution is more sensitive to heat transfer coefficient in alloys with seaweed structure.

3.5. Solidification pattern formation

Fig. 10 shows the dendritic morphology of the investigated alloys at different cooling conditions when the α-phase fraction in the simulation system is 30%. It can be seen that at $h = 0.5$ W/cm^{2}K, different morphologies are formed for different alloys. In the case of alloys with 3 and 8.4 at% Cu, tip splitting occurs during the solidification and results in seaweed structure formation, a common phenomenon during solidification of alloys with weak CM interfacial energy anisotropy [20–23,26,27,34,35,102–104]. While, in alloys with 6 and 10.6 at% Cu, dendritic solidification takes place without any tip splitting. By increasing the heat transfer coefficient to 2 and 4 W/cm^{2}K, the only change in the microstructure of alloys with 6 and 10.6 at% Cu is reduction of dendrite arm spacings, while two other alloys experience significant changes in the morphology of dendrites. CM interfacial energy anisotropy of Al-6 and Al-10.6 at% Cu are equal to 0.0122 and 0.0071, respectively, which are considerably higher than Al-3 at% ($\varepsilon_4 = 0.0035$) and Al-8.4 at% Cu ($\varepsilon_4 = 0.0028$). These results imply that weak interfacial energy anisotropy is the root of sensitivity to cooling conditions, which is in agreement with the results of other studies [31].

Since the anisotropy of CM interfacial energy is high for Al-6 and Al-10.6 at% Cu alloys, dendritic growth is dominant in these alloys at all investigated cooling conditions. On the other hand, in the case of Al-3 and Al-8.4 at% Cu, the anisotropy of interfacial energy is much lower, which results in the formation of different seaweed structures like degenerate or fractal seaweed (FS) [21,34], and compact seaweed (CS) [21] at different cooling conditions.

Fig. 10 (a–c) show the structures of solidifying Al-3 at% Cu at different cooling conditions. In Fig. 10(a), the structure is a mixture of dendrite and fractal seaweed. Dendritic structure is dominant in the initial stages of solidification and the structure trans-

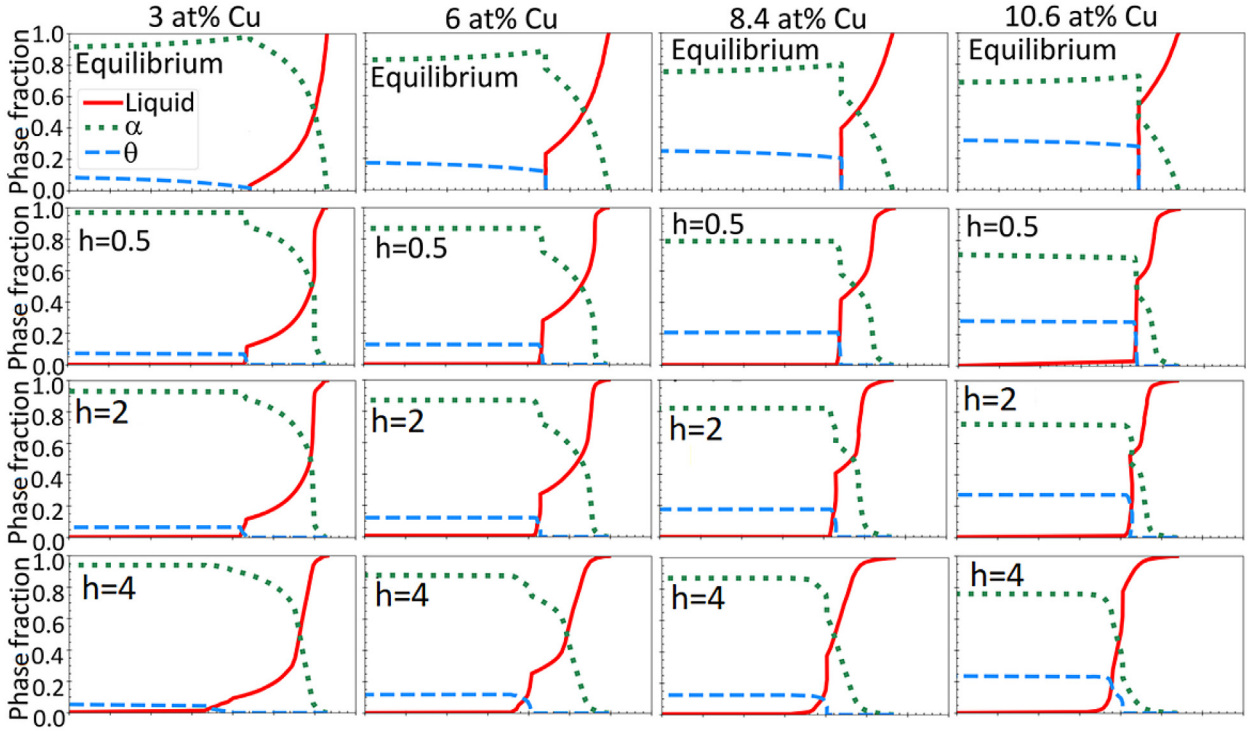

Fig. 8. Effect of heat transfer coefficient, h (W/cm^{2}K), and Cu content (at%) on solidification path of Al-Cu alloys.

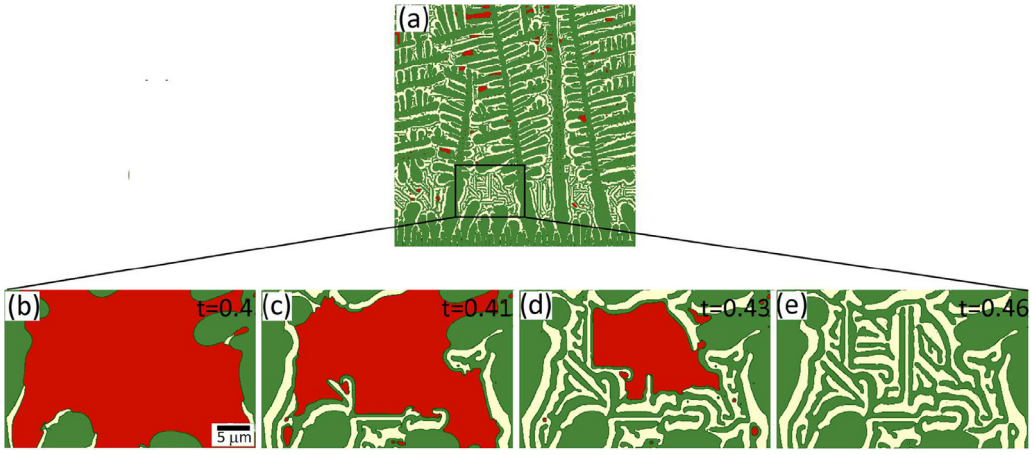

Fig. 9. (a) The solidified structure of Al-10.6 at% Cu solidified at h = 0.5 W/cm^{2}K. (b–e) different snapshots that show the sequence of eutectic structure formation via eutectic reaction. Red, green and white colors denote liquid, α, and θ phases, respectively.

forms into seaweed in the middle of the domain. This transition is due to increase in constitutional supercooling and will be discussed later. By increasing the heat transfer coefficient, transition from dendritic to seaweed structure takes place much sooner. At h = 2 W/cm^{2}K (Fig. 10(b)), the tip splits to alternate sides producing tips of comparable size which grow as main branches and the splitting will keep happening in each one of them. This structure is called degenerate seaweed or FS which is formed by alternating tip splitting [21,34,102] and is characterized by a self-similar internal structure. In other words, similar patterns recur at progressively smaller scales. The same structure is formed at h = 4 W/cm^{2}K (Fig. 10(c)) but the tip splitting frequency (f) is much higher. It has been shown that the tip splitting frequency in FS structure is related to growth velocity (V) as a power law $f = 0.004 \times V^{1.5}$ [34,102]. In this study, at h = 2 and 4 W/cm^{2}K, f is 334 and 538 s^{-1}, respectively, and the related steady state growth velocities are 2900 and 6100 μm/s. The obtained exponent in this study is equal to 1.421 and 1.355 for V = 2900 μm/s and V = 6100 μm/s, respectively. The tip splitting frequency was measured by counting the number of times that the tip splits in a single branch and dividing it by the total time of simulation.

Fig. 10 (g–i) show structures of solidifying Al-8.4 at% Cu at investigated cooling conditions. At h = 0.5 W/cm^{2}K (Fig. 10(g)), a mixture of dendritic and FS is observed. By increasing the heat transfer coefficient to 2 W/cm^{2}K (Fig. 10(h)), tip splitting takes place in a nonfractal mode, which results in a structure known as compact seaweed morphology [21,24,27] or dense branching. This structure is characterized by its subsidiary (secondary) branches that are modulated by leading branch tips [104]. With a further increase in heat transfer to 4 W/cm^{2}K, CS forms with a higher splitting frequency.

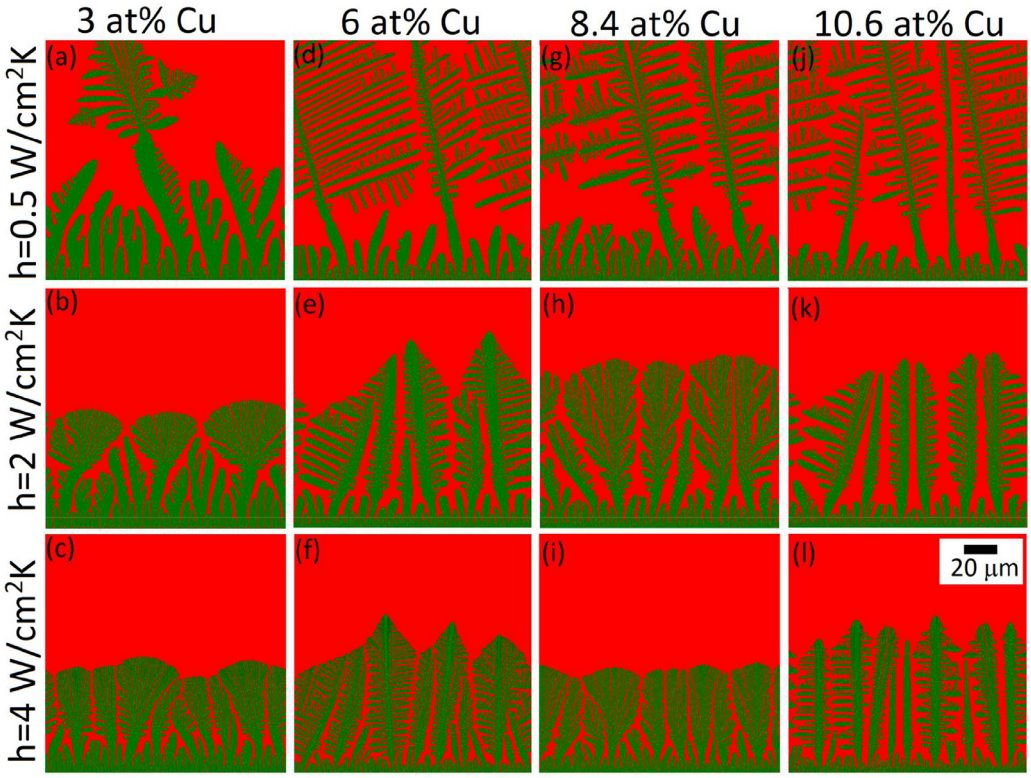

Fig. 10. Morphology of solidifying α-phase for investigated alloys at different cooling condition when solid phase fraction is 30%. Red and green colors denote liquid and α phases, respectively.

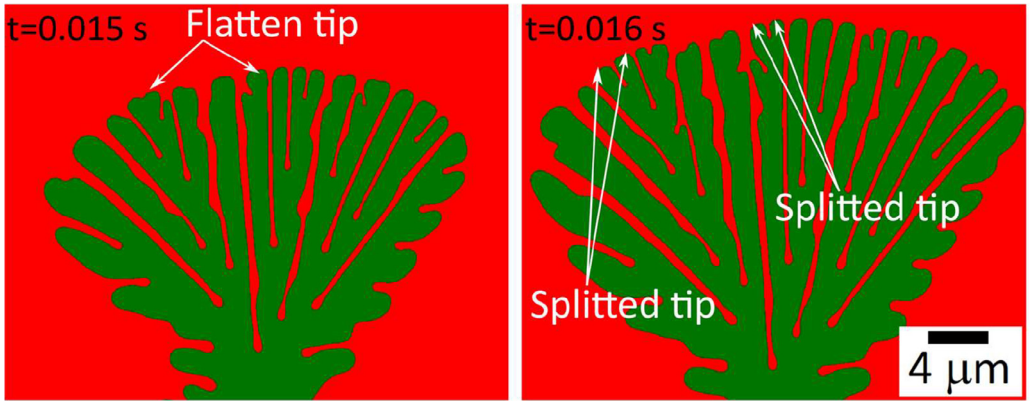

Fig. 11. Tip flattening and splitting phenomena during solidification of Al-3 at% Cu at $h = 0.5$ W/cm^{2}K. Red and green colors denote liquid and α phases, respectively.

During the solidification, dendrites tend to grow in the direction of maximum CM interfacial energy. On the other hand, thermal noise can lead to the destabilization of interface and formation of seaweed structures [25,27]. When the strength of CM interfacial energy is high, the interface is stable against thermal noises and dendritic morphology with a parabolic tip is dominant, which is the case for Al-6 and Al-10.6 at% Cu. In the case of Al-3 and Al-8.4 at% Cu, the interfacial energy anisotropy is low, and interface destabilizes due to the thermal noise and consequently tip flattens and widens before splitting (Fig. 11). The details of the tip flattening and splitting mechanisms have been discussed elsewhere [21–23,27,34,102].

As it was elucidated, FS is dominant in Al-3 at% Cu and CS is the dominant structure in Al-8.4 at% Cu, while the strength of interfacial energy anisotropy is weak in both. This difference stems from different constitutional supercooling during solidification. Fig. 12(a) and (b) show concentration profile and corresponding liquidus line at ahead of growing seaweed for Al-3 and Al-8.4 at% Cu, respectively, for the heat transfer coefficient of 4 W/cm^{2}K. For Al-3 at% Cu, the constitutional supercooling is 5.1 K exactly at ahead of growing tip and increases to almost 25 K in 6 μm from it. For Al-8.4 at% Cu supercooling is 9.85 K ahead of growing tip and reaches 68 K in 9 μm. At the limit of diffusion control growth, it has been shown that when the interfacial energy anisotropy and supercooling are both small, FS is dominant and, as supercooling increases, a transition is observed and CS becomes the dominant structure [24,27].

In addition to the formation of different patterns in different alloys, it can be seen in Fig. 10 (a–c) and Fig. 10 (g–i) that there is a pattern transition from dendritic to seaweed structure in alloys with low interfacial energy anisotropy (Al-3 at% and Al-8.4 at% Cu), and depending on the value of heat transfer coefficient, this transition takes place at different times. But in the case of alloys with high interfacial energy anisotropy, den-

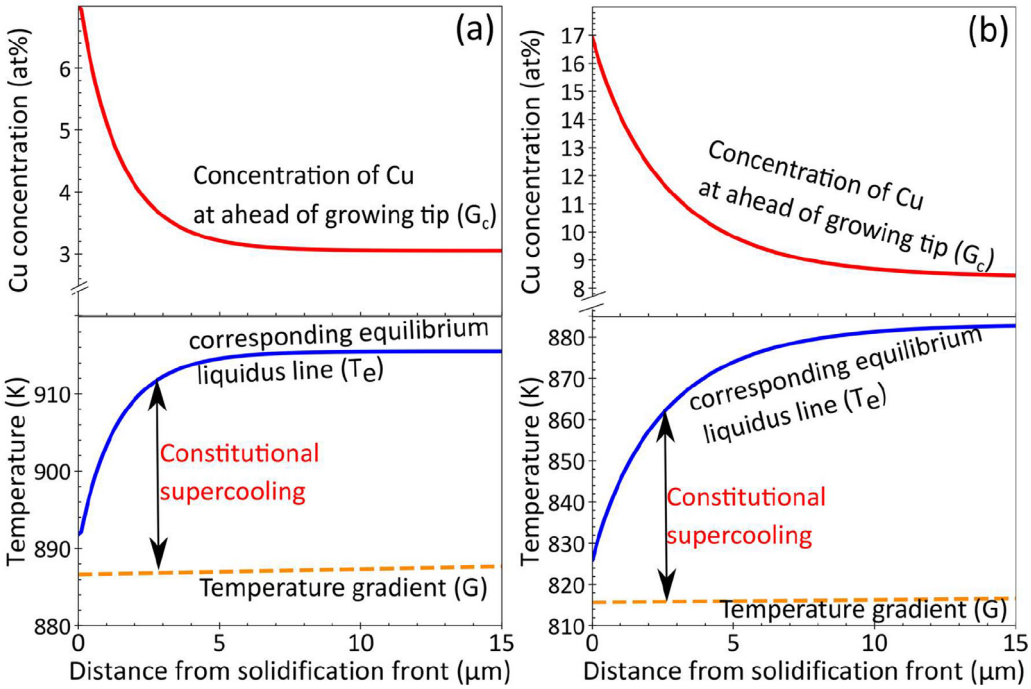

Fig. 12. Concentration profile ahead of growing tip and corresponding constitutional supercooling for (a) Al-3 at% Cu, and (b) Al-8.4 at% Cu.

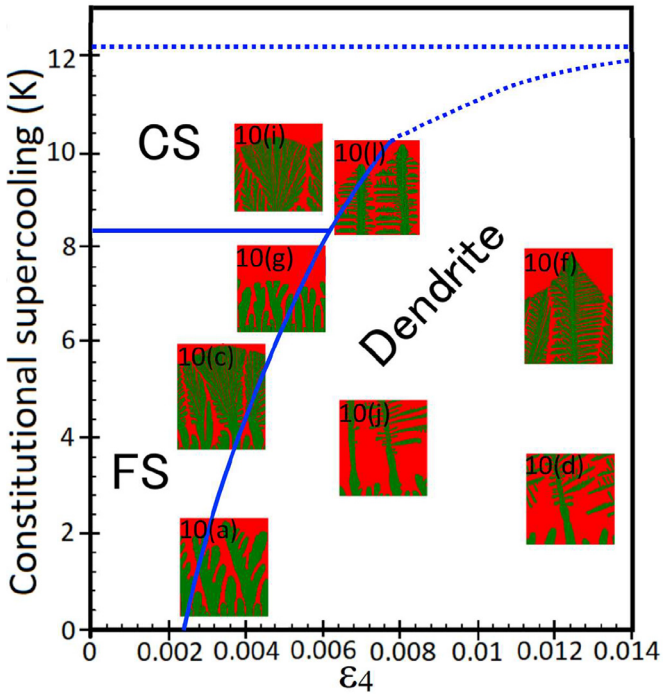

Fig. 13. Map of morphology formation in Δ-ε_4 plane during solidification of Al-Cu alloys. The dotted lines show the expected trends at higher constitutional supercooling. Inset figures are correlated to microstructures in Fig. 10 (a–l). Red and green colors denote liquid and α phases, respectively.

dritic structure is the only stable structure. The underlying reason for the pattern transition in alloys with low interfacial energy anisotropy is the change in constitutional supercooling while solidification proceeds. At initial stage of solidification, supercooling is low and a dendritic structure forms. By increasing the solidification time, constitutional supercooling reaches a critical value that triggers tip splitting and seaweed structure formation. At higher heat transfer coefficients, supercooling reaches the critical value sooner and the pattern transition takes place sooner. For example, in the case of Al-3 at% Cu when $h = 4$ W/cm^{2}K, constitutional supercooling is lower than 1.9 K in the first 0.014 s and dendritic microstructure forms. After this point, constitutional supercooling reaches 2.8 K and the first splitting takes place. As solidification time increases, the constitutional supercooling increases to 5.2 K and remains constant. In the case of $h = 2$ W/cm^{2}K, it takes 0.3 s for the constitutional supercooling to reach its critical value (2.9 K), which results in a transition from dendritic to seaweed.

Based on the patterns obtained from phase-field simulations and considering the aforementioned analysis, we construct a map of the anisotropy parameter strength (ε_4) versus constitutional supercooling (Δ) in Fig. 13 that shows solidification morphology formation in Al-Cu alloys. Regardless of Cu content and supercooling, when the anisotropy parameter value is larger than 0.004, dendritic morphology is dominant and seaweed structure is halted. At a lower anisotropy and supercooling less than 8 K, fractal seaweed forms during solidification. Compact seaweed structure is dominant at anisotropies less than 0.005 and supercooling greater than 8 K.

4. Conclusions

Solidification of four Al-Cu alloys with 3%, 6%, 8.4%, and 10.6 at% Cu was investigated using atomistic-informed multi-phase field modeling. We investigated the combined effects of cooling condition, alloy composition and interfacial energy anisotropy on θ-phase fraction and its distribution, and growth dynamics and morphology of solidification structures. First, the CM interfacial energies and its anisotropy were determined using molecular dynamic simulations. These values were used in phase-field simulations to quantitatively investigate the interactive effects of Cu content, CM interfacial properties, and cooling conditions on growth dynamics and solidification patterns. Specific findings include the following:

1. Molecular dynamics simulation results showed that the CM interfacial energy decreases linearly with increasing Cu content, while its anisotropy does not show a specific trend.

2. Phase-field simulation results showed that with increasing the cooling rate, the dendrite arm spacing and the amount of θ-phase decrease, and this reduction is more pronounced in alloys with higher Cu content. Also, the θ-phase fraction decreases as the heat transfer coefficient increases. This reduction is due to the higher supercooling needed for eutectic reaction, which results in the formation of higher α-phase, and less liquid transforms into α+θ phase via eutectic reaction. Furthermore, the coring phenomenon is more noticeable at higher cooling rates, which results in a reduction in Cu content in the interdendritic regions and a decrease in θ-phase.
3. Distribution of θ-phase is more homogenous in alloys with seaweed structures (Al-3 and Al-8.4 at% Cu) than the alloys with dendritic structures. In all investigated alloys, the distribution of θ-phase becomes more homogenous by increasing the heat transfer coefficient, but it is more sensitive to the value of heat transfer coefficient with seaweed structures.
4. Anisotropy of CM interfacial energy has a significant effect on solidification patterns and their growth dynamics. At the limit of diffusion control growth, when the strength of anisotropy is higher than 0.005 dendritic morphology is dominant at all cooling rates. At lower CM interfacial energy anisotropy different seaweed structures can form regarding constitutional supercooling ahead of the growing tip. When supercooling is less than 8 K, degenerate or fractal seaweed form while at higher supercoolings compact seaweed is dominant microstructure.

Declaration of Competing Interest

The authors declare that they have no known competing financial interests or personal relationships that could have appeared to influence the work reported in this paper.

Data availability

All necessary data generated or analyzed during this study are included in this published article, and other auxiliary data are available from the corresponding author on reasonable request.

CRediT authorship contribution statement

Ghavam Azizi: Conceptualization, Methodology, Software, Formal analysis, Writing – original draft. **Sepideh Kavousi:** Conceptualization, Methodology, Formal analysis, Writing – review & editing. **Mohsen Asle Zaeem:** Supervision, Conceptualization, Methodology, Formal analysis, Writing – review & editing, Funding acquisition.

Acknowledgment

This study was supported by the National Science Foundation, NSF-CMMI 2031800, and by NASA, 80NSSC19K0569. We are grateful for supercomputing time allocation provided by the Extreme Science and Engineering Discovery Environment (XSEDE), Award No. TG-DMR140008.

Appendix 1

Eq. (A.1) was used to calculate the anisotropy parameters in 3D:

$$\gamma\left(\hat{n}\right)=\gamma_{0(3D)}\left[1+\delta_1\left(4\sum_{i=1}^{3}n_i^4-3\right)+\delta_2\left(\sum_{i=1}^{3}n_i^6+30n_1^2n_2^2n_3^2\right)\right]. \tag{A.1}$$

The following 2D equation (Eq. (A.2)) is used for PF simulations:

$$\gamma=\gamma_{0(2D)}(1+\varepsilon_4(\cos 4\varphi)) \tag{A.2}$$

Using a series of trigonometric relations, we can calculate ε_4 in 2D as a function of δ_1 and δ_2. Having $n_1=\cos\varphi$, $n_2=\sin\varphi$, and $n_3=0$, we can rewrite Eq. (A.1) as follow:

$$\frac{\gamma\left(\hat{n}\right)}{\gamma_{0(3D)}}=\left[1+4\delta_1\left(\cos^4\varphi+\sin^4\varphi-3/4\right)+\delta_2\left(\cos^6\varphi+\sin^6\varphi\right)\right] \tag{A.3}$$

From trigonometric relations we have:

$$\cos^4\varphi+\sin^4\varphi=\left(\cos^2\varphi+\sin^2\varphi\right)^2-2\sin^2\varphi\cos^2\varphi=1-2\sin^2\varphi\cos^2\varphi \tag{A.4}$$

$$\cos^6\varphi+\sin^6\varphi=\left(\cos^2\varphi+\sin^2\varphi\right)^3-3\sin^2\varphi\cos^2\varphi=1-3\sin^2\varphi\cos^2\varphi \tag{A.5}$$

$$\sin\varphi\cos\varphi=\frac{1}{2}\sin 2\varphi\Rightarrow\sin^2\varphi\cos^2\varphi=\frac{1}{4}\sin^2 2\varphi \tag{A.6}$$

$$sin^2 2\varphi=\frac{1-\cos 4\varphi}{2}. \tag{A.7}$$

By substituting Eqs. (A.4)–(A.7) into Eq. (A.3) we have:

$$\frac{\gamma\left(\hat{n}\right)}{\gamma_{0(3D)}}=\left[1+4\delta_1\left(1-\frac{1}{4}+\frac{1}{4}\cos 4\varphi-\frac{3}{4}\right)+\delta_2\left(\frac{5}{8}+\frac{3}{8}\cos 4\varphi\right)\right] \tag{A.8}$$

Then:

$$\frac{\gamma\left(n^{\hat{n}}\right)}{\gamma_{0(3D)}}=1+\frac{5}{8}\delta_2+\left(\delta_1+\frac{3}{8}\delta_2\right)\cos 4\varphi. \tag{A.9}$$

We define $X=1+\frac{5}{8}\ \delta_2$ and $Y=\delta_1+\frac{3}{8}\delta_2$ and divide all terms by X. then we have:

$$\frac{\gamma\left(\hat{n}\right)}{\gamma_{0(3D)}X}=1+\frac{Y}{X}\cos 4\varphi. \tag{A.10}$$

Comparing Eqs. (A.2) and (A.10) we have $\varepsilon_4=\frac{Y}{X}$ and $\gamma_{0(2D)}=\gamma_{0(3D)}X$. Since $X\sim1$ for all alloys, $\gamma_{0(2D)}=\gamma_{0(3D)}$.

Appendix 2

The analytical solutions for λ_1 and λ_2 Eqs. (13) and (14) include material properties which are obtained from MD simulations and Thermo-Calc databases. The first parameter is Gibbs-Thomson coefficient which is calculated using Eq. (A.11).

$$\Gamma_{sl}=\frac{\gamma_{sl}+\gamma''_{sl}}{\rho\Delta s_f} \tag{A.11}$$

where γ_{sl} and γ''_{sl} are CM interfacial energy and its second derivative, respectively. ρ is density and Δs_f is the entropy of fusion. Almost all the dendrites of investigated Al-Cu alloys have ⟨100⟩ [001] orientation. So, based on Table 1 we can use Eq. (A.12) to calculate numerator of Eq. (A.11).

$$\gamma_{sl}+\gamma''_{sl}=\gamma_0(1-15\delta_1-5\delta_2) \tag{A.12}$$

Entropy of fusion, Δs_f, is extracted from Thermo-Calc simulations and $\rho=\frac{wt\%_{Al}+wt\%_{Cu}}{V}$ where $wt\%_{Al}$and $wt\%_{Cu}$ are weight percent of Al and Cu, respectively. V is the volume of 1 kg alloy and is calculated as: $V=(\frac{wt\%_{Al}}{\rho_{Al}})+(\frac{wt\%_{Cu}}{\rho_{Cu}})$. ρ_{Al} and ρ_{Cu} are equal to 2710 kg/m^3 and 8950 kg/m^3, respectively.

Table A.1
Material properties of investigated alloys.

(at%)	c_0(wt%)	c_{eut}(wt%)	$\Delta T_0(K)$	m_l(K/wt%)	$\tilde{D}^{Al}_{CuCu}$(m^2/s)	Δs_f(J/K.kg)	ρ(kg/m^3)	$\gamma_{sl}+\gamma''_{sl}$(J/m^2)	Γ_{sl}(K.m)
3	6.9	33.49	99	−3.07	5.12E-09	551	2847	0.104	6.63E-08
6	13	33.49	77	−2.93	5.05E-09	541.73	2980	0.0779	4.83E-08
8.4	17.76	33.49	63	−2.91	4.9E-09	512.29	3092	0.0832	5.25E-08
10.6	21.83	33.49	50	−2.89	4.88E-09	484.11	3196	0.0799	5.16E-08

Table A.2
Process dependent parameters of investigated alloys at different heat transfer coefficients.

Cu (at%)	h (W/cm^2.K)	v^* (m/s)	$G \times 10^3$(K/m)	λ_1 (μm)	λ_2 (μm)
3	0.5	0.0024	19.9	107.5	13.7
	2	0.0029	73.5	53.6	8.5
	4	0.0061	16.5	29.7	5
6	0.5	0.0027	21.6	86.9	9.83
	2	0.0038	74.2	43	5.9
	4	0.0072	17.3	24	3.7
8.4	0.5	0.0027	25.2	76.5	8.6
	2	0.0035	75.05	41.6	5.4
	4	0.0068	17.3	23.2	3.3
10.6	0.5	0.0027	29.3	66.5	7.3
	2	0.0037	79.6	37.3	4.7
	4	0.0069	175	21.5	2.93

Interdiffusion coefficient of Cu atoms at the liquidus temperatures ($\tilde{D}^{Al}_{CuCu}$), freezing range (ΔT_0), slope of liquidus line (m_l), and final composition of liquid before freezing (c_{eut}) are extracted from Thermo-Calc. All these parameters are presented in Table A.1.

Interface velocity (v^*) and temperature gradient (G) were extracted from phase-field simulations at steady state condition and are presented in Table A.2. Also, in this study the equilibrium partition coefficient, $k_e = 0.185$, is used.

References

[1] L. Wang, J.J. Hoyt, N. Wang, N. Provatas, C.W. Sinclair, Controlling solid-liquid interfacial energy anisotropy through the isotropic liquid, Nat. Commun. 11 (1) (2020) 1–7.
[2] S.H. Davis, Theory of Solidification, Cambridge University Press, New York, 2001.
[3] J.A. Dantzig, M. Rappaz, Solidification: -Revised & Expanded, EPFL Press, New York, 2016.
[4] M.E. Glicksman, Principles of Solidification: an Introduction to Modern Casting and Crystal Growth Concepts, Springer Science & Business Media, New York, 2010.
[5] J. Yang, W. Hu, Nucleation and solid–liquid interfacial energy of Li nanoparticles: a molecular dynamics study, Phys. Status Solidi (b) 253 (10) (2016) 1941–1946.
[6] Y. Shibuta, S. Sakane, E. Miyoshi, S. Okita, T. Takaki, M. Ohno, Heterogeneity in homogeneous nucleation from billion-atom molecular dynamics simulation of solidification of pure metal, Nat. Commun. 8 (1) (2017) 1–9.
[7] M. Rappaz, J. Friedli, A. Mariaux, M. Salgado-Ordorica, The influence of solid–liquid interfacial energy anisotropy on equilibrium shapes, nucleation, triple lines and growth morphologies, Scr. Mater. 62 (12) (2010) 904–909.
[8] W.J. Boettinger, S.R. Coriell, A. Greer, A. Karma, W. Kurz, M. Rappaz, R. Trivedi, Solidification microstructures: recent developments, future directions, Acta Mater. 48 (1) (2000) 43–70.
[9] J.S. Langer, Instabilities and pattern formation in crystal growth, Rev. Mod. Phys. 52 (1) (1980) 1.
[10] J. Hoyt, M. Asta, T. Haxhimali, A. Karma, R. Napolitano, R. Trivedi, B.B. Laird, J.R. Morris, Crystal–melt interfaces and solidification morphologies in metals and alloys, MRS Bull. 29 (12) (2004) 935–939.
[11] T. Haxhimali, A. Karma, F. Gonzales, M. Rappaz, Orientation selection in dendritic evolution, Nat. Mater. 5 (8) (2006) 660–664.
[12] S. Coriell, R. Sekerka, The effect of the anisotropy of surface tension and interface kinetics on morphological stability, J. Cryst. Growth 34 (2) (1976) 157–163.
[13] P. Kopczyński, W.J. Rappel, A. Karma, Critical role of crystalline anisotropy in the stability of cellular array structures in directional solidification, Phys. Rev. Lett. 77 (16) (1996) 3387.
[14] A.A. Golovin, S.H. Davis, Effect of anisotropy on morphological instability in the freezing of a hypercooled melt, Phys. D 116 (3–4) (1998) 363–391.
[15] R. Trivedi, Effects of anisotropy properties on interface pattern formation, Appl. Mech. Rev. 43 (55) (1990) S79–S84.
[16] W.W. Mullins, R. Sekerka, Stability of a planar interface during solidification of a dilute binary alloy, J. Appl. Phys. 35 (2) (1964) 444–451.
[17] G. Young, S. Davis, K. Brattkus, Anisotropic interface kinetics and tilted cells in unidirectional solidification, J. Cryst. Growth 83 (4) (1987) 560–571.
[18] H. Xing, L. Zhang, K. Song, H. Chen, K. Jin, Effect of interface anisotropy on growth direction of tilted dendritic arrays in directional solidification of alloys: insights from phase-field simulations, Int. J. Heat Mass Transf. 104 (2017) 607–614.
[19] F. Yu, Y. Wei, Effect of surface tension anisotropy and welding parameters on initial instability dynamics during solidification: a phase-field study, Metall. Mater. Trans. A 49 (8) (2018) 3293–3305.
[20] T. Ihle, H. Müller-Krumbhaar, Diffusion-limited fractal growth morphology in thermodynamical two-phase systems, Phys. Rev. Lett. 70 (20) (1993) 3083.
[21] T. Ihle, H. Müller-Krumbhaar, Fractal and compact growth morphologies in phase transitions with diffusion transport, Phys. Rev. E 49 (4) (1994) 2972.
[22] S. Akamatsu, G. Faivre, T. Ihle, Symmetry-broken double fingers and seaweed patterns in thin-film directional solidification of a nonfaceted cubic crystal, Phys. Rev. E 51 (5) (1995) 4751.
[23] M. Georgelin, A. Pocheau, Onset of sidebranching in directional solidification, Phys. Rev. E 57 (3) (1998) 3189.
[24] E. Brener, H. Müller-Krumbhaar, D. Temkin, Kinetic phase diagram and scaling relations for stationary diffusional growth, EPL Europhys. Lett. 17 (6) (1992) 535.
[25] E. Brener, T. Ihle, H. Müller-Krumbhaar, Y. Saito, K. Shiraishi, Fluctuation effects on dendritic growth morphology, Phys. A 204 (1–4) (1994) 96–110.
[26] S. Akamatsu, G. Faivre, Anisotropy-driven dynamics of cellular fronts in directional solidification in thin samples, Phys. Rev. E 58 (3) (1998) 3302.
[27] E. Brener, H. Müller-Krumbhaar, D. Temkin, Structure formation and the morphology diagram of possible structures in two-dimensional diffusional growth, Phys. Rev. E 54 (3) (1996) 2714.
[28] S. Kavousi, A. Gates, L. Jin, M. Asle Zaeem, A temperature-dependent atomistic-informed phase-field model to study dendritic growth, Journal of Crystal Growth 579 (2022) 126461.
[29] S. Kavousi, B.R. Novak, D. Moldovan, M. Asle Zaeem, Quantitative prediction of rapid solidification by integrated atomistic and phase-field modeling, Acta Materialia 211 (2021) 116885.
[30] S. Kavousi, M. Asle Zaeem, Quantitative phase-field modeling of solute trapping in rapid solidification, Acta Materialia 205 (2021) 116562.
[31] M. Amoorezaei, S. Gurevich, N. Provatas, Orientation selection in solidification patterning, Acta Mater. 60 (2) (2012) 657–663.
[32] H. Xing, X. Dong, H. Wu, G. Hao, J. Wang, C. Chen, K. Jin, Degenerate seaweed to tilted dendrite transition and their growth dynamics in directional solidification of non-axially oriented crystals: a phase-field study, Sci. Rep. 6 (2016) 26625.
[33] H. Xing, M. Ji, X. Dong, Y. Wang, L. Zhang, S. Li, Growth competition between columnar dendrite and degenerate seaweed during directional solidification of alloys: insights from multi-phase field simulations, Mater. Des. 185 (2020) 108250.
[34] B. Utter, E. Bodenschatz, Dynamics of low anisotropy morphologies in directional solidification, Phys. Rev. E 66 (5) (2002) 051604.
[35] Y. Chen, B. Billia, D.Z. Li, H. Nguyen-Thi, N.M. Xiao, A.A. Bogno, Tip-splitting instability and transition to seaweed growth during alloy solidification in anisotropically preferred growth direction, Acta Mater. 66 (2014) 219–231.
[36] G.W. Lee, S. Jeon, C. Park, D.H. Kang, Crystal–liquid interfacial free energy and thermophysical properties of pure liquid Ti using electrostatic levitation: hypercooling limit, specific heat, total hemispherical emissivity, density, and interfacial free energy, J. Chem. Thermodyn. 63 (2013) 1–6.
[37] J.Q. Broughton, G.H. Gilmer, Molecular dynamics of the crystal–fluid interface. v. structure and dynamics of crystal–melt systems, J. Chem. Phys. 84 (10) (1986) 5749–5758.
[38] J. Hoyt, M. Asta, A. Karma, Method for computing the anisotropy of the solid-liquid interfacial free energy, Phys. Rev. Lett. 86 (24) (2001) 5530.
[39] J. Hoyt, M. Asta, Atomistic computation of liquid diffusivity, solid-liquid interfacial free energy, and kinetic coefficient in Au and Ag, Phys. Rev. B 65 (21) (2002) 214106.
[40] D. Sun, M. Asta, J. Hoyt, Kinetic coefficient of Ni solid-liquid interfaces from molecular-dynamics simulations, Phys. Rev. B 69 (2) (2004) 024108.
[41] E. Asadi, M. Asle Zaeem, The anisotropy of hexagonal close-packed and liquid interface free energy using molecular dynamics simulations based on modified embedded-atom method, Acta Mater. 107 (2016) 337–344.

[42] E. Asadi, M. Asle Zaeem, S. Nouranian, M.I. Baskes, Quantitative modeling of the equilibration of two-phase solid-liquid Fe by atomistic simulations on diffusive time scales, Phys. Rev. B 91 (2) (2015) 024105.
[43] E. Asadi, M. Asle Zaeem, S. Nouranian, M.I. Baskes, Two-phase solid–liquid coexistence of Ni, Cu, and Al by molecular dynamics simulations using the modified embedded-atom method, Acta Mater. 86 (2015) 169–181.
[44] S. Kavousi, B.R. Novak, M. Asle Zaeem, D. Moldovan, Combined molecular dynamics and phase field simulation investigations of crystal-melt interfacial properties and dendritic solidification of highly undercooled titanium, Comput. Mater. Sci. 163 (2019) 218–229.
[45] R. Ramakrishnan, R. Sankarasubramanian, Crystal-melt kinetic coefficients of Ni3Al, Acta Mater. 127 (2017) 25–32.
[46] S. Kavousi, B.R. Novak, M.I. Baskes, M. Asle Zaeem, D. Moldovan, Modified embedded-atom method potential for high-temperature crystal-melt properties of Ti–Ni alloys and its application to phase field simulation of solidification, Model. Simul. Mater. Sci. Eng. 28 (1) (2019) 015006.
[47] A. Mahata, T. Mukhopadhyay, M. Asle Zaeem, Modified embedded-atom method interatomic potentials for Al-Cu, Al-Fe and Al-Ni binary alloys: from room temperature to melting point, Comput. Mater. Sci. 201 (2022) 110902.
[48] C. Becker, D. Olmsted, M. Asta, J. Hoyt, S. Foiles, Atomistic underpinnings for orientation selection in alloy dendritic growth, Phys. Rev. Lett. 98 (12) (2007) 125701.
[49] M. Asta, J. Hoyt, A. Karma, Calculation of alloy solid-liquid interfacial free energies from atomic-scale simulations, Phys. Rev. B 66 (10) (2002) 100101.
[50] A. Potter, J. Hoyt, A molecular dynamics simulation study of the crystal–melt interfacial free energy and its anisotropy in the Cu–Ag–Au ternary system, J. Cryst. Growth 327 (1) (2011) 227–232.
[51] J. Friedli, J. Fife, P. Di Napoli, M. Rappaz, Dendritic growth morphologies in Al-Zn alloys—Part I: x-ray tomographic microscopy, Metall. Mater. Trans. A 44 (12) (2013) 5522–5531.
[52] J. Dantzig, P. Di Napoli, J. Friedli, M. Rappaz, Dendritic growth morphologies in Al-Zn alloys—Part II: phase-field computations, Metall. Mater. Trans. A 44 (12) (2013) 5532–5543.
[53] F. Gonzales, M. Rappaz, Dendrite growth directions in aluminum-zinc alloys, Metall. Mater. Trans. A 37 (9) (2006) 2797–2806.
[54] M. Becker, J. Dantzig, M. Kolbe, S.T. Wiese, F. Kargl, Dendrite orientation transition in AlGe alloys, Acta Mater. 165 (2019) 666–677.
[55] J. Hoyt, S. Raman, N. Ma, M. Asta, Unusual temperature dependence of the solid-liquid interfacial free energy in the Cu-Zr system, Comput. Mater. Sci. 154 (2018) 303–308.
[56] C. Qi, B. Xu, L. Kong, J. Li, Solid-liquid interfacial free energy and its anisotropy in the Cu-Ni binary system investigated by molecular dynamics simulations, J. Alloy. Compd. 708 (2017) 1073–1080.
[57] G. Kaptay, On the solid/liquid interfacial energies of metals and alloys, J. Mater. Sci. 53 (5) (2018) 3767–3784.
[58] J. Rahman, Atomistic simulations for computing solid liquid interface properties of the Al-Mg system, Master's Thesis, McMaster University, 2009.
[59] S. Plimpton, Fast parallel algorithms for short-range molecular dynamics, J. Comput. Phys. 117 (1) (1995) 1–19.
[60] A. Mahata, M. Asle Zaeem, Effects of solidification defects on nanoscale mechanical properties of rapid directionally solidified Al-Cu Alloy: a large scale molecular dynamics study, J. Cryst. Growth 527 (2019) 125255.
[61] A. Mahata, M. Asle Zaeem, M.I. Baskes, Understanding homogeneous nucleation in solidification of aluminum by molecular dynamics simulations, Model. Simul. Mater. Sci. Eng. 26 (2) (2018) 025007.
[62] A. Mahata, M. Asle Zaeem, Size effect in molecular dynamics simulation of nucleation process during solidification of pure metals: investigating modified embedded atom method interatomic potentials, Model. Simul. Mater. Sci. Eng. 27 (8) (2019) 085015.
[63] S. Kavousi, B.R. Novak, J. Hoyt, D. Moldovan, Interface kinetics of rapid solidification of binary alloys by atomistic simulations: application to Ti-Ni alloys, Comput. Mater. Sci. 184 (2020) 109854.
[64] J. Eiken, B. Böttger, I. Steinbach, Multiphase-field approach for multicomponent alloys with extrapolation scheme for numerical application, Phys. Rev. E 73 (6) (2006) 066122.
[65] MICRESS User Guide, Version 6.4, Volume 2: Running MICRESS. https://micress.rwth-aachen.de/files/documentation/Vol2_Running_MICRESS.pdf
[66] J. Eiken, Phase-field simulation of microstructure formation in technical magnesium alloys, Int. J. Mater. Res. 101 (4) (2010) 503–509.
[67] B. Böttger, J. Eiken, I. Steinbach, Phase field simulation of equiaxed solidification in technical alloys, Acta Mater. 54 (10) (2006) 2697–2704.
[68] M. Gündüz, J. Hunt, The measurement of solid-liquid surface energies in the Al-Cu, Al-Si and Pb-Sn systems, Acta Metall. 33 (9) (1985) 1651–1672.
[69] V. Kokotin, U. Hecht, Molecular dynamics simulations of Al–Al_2Cu phase boundaries, Comput. Mater. Sci. 86 (2014) 30–37.
[70] J. Eiken, Numerical solution of the phase-field equation with minimized discretization error, in: Proceedings of theIOP Conference Series Materials Science and Engineering, 2012.
[71] A. Carré, B. Böttger, M. Apel, Implementation of an antitrapping current for a multicomponent multiphase-field ansatz, J. Cryst. Growth 380 (2013) 5–13.
[72] M. Leitner, T. Leitner, A. Schmon, K. Aziz, G. Pottlacher, Thermophysical properties of liquid aluminum, Metall. Mater. Trans. A 48 (6) (2017) 3036–3045.
[73] S. Choi, H. Cho, S. Kumai, Effect of the precipitation of secondary phases on the thermal diffusivity and thermal conductivity of Al-4.5 Cu alloy, J. Alloy. Compd. 688 (2016) 897–902.
[74] J. Zhao, Y. Yuan, F. Cui, Relationship between the Cu content and thermal properties of Al–Cu alloys for latent heat energy storage, J. Therm. Anal. Calorim. 129 (1) (2017) 109–115.
[75] D. Du, H. Zhang, D.J. Srolovitz, Properties and determination of the interface stiffness, Acta Mater. 55 (2) (2007) 467–471.
[76] A.S. Barros, I.A. Magno, F.A. Souza, C.A. Mota, A.L. Moreira, M.A. Silva, O.L. Rocha, Measurements of microhardness during transient horizontal directional solidification of Al-Rich Al-Cu alloys: effect of thermal parameters, primary dendrite arm spacing and Al 2 Cu intermetallic phase, Met. Mater. Int. 21 (3) (2015) 429–439.
[77] K. Young, D. Kerkwood, The dendrite arm spacings of aluminum-copper alloys solidified under steady-state conditions, Metall. Trans. A 6 (1) (1975) 197–205.
[78] J. Sarreal, G. Abbaschian, The effect of solidification rate on microsegregation, Metall. Trans. A 17 (11) (1986) 2063–2073.
[79] M. Gündüz, E. Çadırlı, Directional solidification of aluminium–copper alloys, Mater. Sci. Eng. A 327 (2) (2002) 167–185.
[80] E.S. Meza, F. Bertelli, P.R. Goulart, N. Cheung, A. Garcia, The effect of the growth rate on microsegregation: experimental investigation in hypoeutectic Al–Fe and Al–Cu alloys directionally solidified, J. Alloy. Compd. 561 (2013) 193–200.
[81] X. Lin, W. Huang, J. Feng, T. Li, Y. Zhou, History-dependent selection of primary cellular/dendritic spacing during unidirectional solidification in aluminum alloys, Acta Mater. 47 (11) (1999) 3271–3280.
[82] J. Kaneko, Dendrite coarsening during solidification of hypo-and hyper-eutectic Al-Cu alloys, J. Mater. Sci. 12 (7) (1977) 1392–1400.
[83] J. Hunt, Solidification and Casting of Metals, The Metal Society, London, 1979.
[84] W. Kurz, D. Fisher, Dendrite growth at the limit of stability: tip radius and spacing, Acta Metall. 29 (1) (1981) 11–20.
[85] Y. Wang, L. Peng, Y. Ji, X. Cheng, C. Wang, Y. Wu, Y. Fu, L.Q. Chen, Effect of cooling rates on the dendritic morphology transition of Mg–6Gd alloy by *in situ* X-ray radiography, J. Mater. Sci. Technol. 34 (7) (2018) 1142–1148.
[86] M. Amoorezaei, S. Gurevich, N. Provatas, Spacing characterization in Al–Cu alloys directionally solidified under transient growth conditions, Acta Mater. 58 (18) (2010) 6115–6124.
[87] M.A. Tschopp, J.D. Miller, A.L. Oppedal, K.N. Solanki, Characterizing the local primary dendrite arm spacing in directionally solidified dendritic microstructures, Metall. Mater. Trans. A 45 (1) (2014) 426–437.
[88] D. McCartney, J. Hunt, Measurements of cell and primary dendrite arm spacings in directionally solidified aluminium alloys, Acta Metall. 29 (11) (1981) 1851–1863.
[89] J. Hunt, S.-.Z. Lu, Numerical modeling of cellular/dendritic array growth: spacing and structure predictions, Metall. Mater. Trans. A 27 (3) (1996) 611–623.
[90] V. Laxmanan, Cellular and primary dendritic spacings in directionally solidified alloys, Scr. Mater. 38 (8) (1998) 1289–1297.
[91] Q. Li, C. Beckermann, Evolution of the sidebranch structure in free dendritic growth, Acta Mater. 47 (8) (1999) 2345–2356.
[92] D. Eskin, Q. Du, D. Ruvalcaba, L. Katgerman, Experimental study of structure formation in binary Al–Cu alloys at different cooling rates, Mater. Sci. Eng. A 405 (1–2) (2005) 1–10.
[93] J.M. Quaresma, C.A. Santos, A. Garcia, Correlation between unsteady-state solidification conditions, dendrite spacings, and mechanical properties of Al-Cu alloys, Metall. Mater. Trans. A 31 (12) (2000) 3167–3178.
[94] D. Liu, L. Zhang, Y. Du, H. Xu, S. Liu, L. Liu, Assessment of atomic mobilities of Al and Cu in fcc Al–Cu alloys, Calphad 33 (4) (2009) 761–768.
[95] W. Kurz, J. Fisher, Fundamentals of Solidification, ed, Trans Tech Publications Ltd., Uetikon-Zuerich, Switzerland, 1998.
[96] D. Bouchard, J.S. Kirkaldy, Prediction of dendrite arm spacings in unsteady-and steady-state heat flow of unidirectionally solidified binary alloys, Metall. Mater. Trans. B 28 (4) (1997) 651–663.
[97] V. Ronté, A. RoÓlSz, The effect of cooling rate and composition on the secondary dendrite arm spacing during solidification. Part I: al-Cu-Si alloys, Int. J. Cast Met. Res. 13 (6) (2001) 337–342.
[98] S. Sahoo, S. Ghosh, Microstructure evolution of eutectic Al–Cu strips by high-speed twin-roll strip casting process, Appl. Phys. A 121 (1) (2015) 45–50.
[99] Q. Lei, J. Wang, A. Misra, Mechanical behavior of Al–Al_2Cu–Si and Al–Al_2Cu eutectic alloys, Crystals 11 (2) (2021) 194.
[100] A.B. Michael, M.B. Bever, Solidification of aluminum-rich aluminum-copper alloys, JOM 6 (1) (1954) 47–56.
[101] J.L. Fattebert, M. Wickett, P. Turchi, Phase-field modeling of coring during solidification of Au–Ni alloy using quaternions and CALPHAD input, Acta Mater. 62 (2014) 89–104.
[102] B. Utter, R. Ragnarsson, E. Bodenschatz, Alternating tip splitting in directional solidification, Phys. Rev. Lett. 86 (20) (2001) 4604.
[103] S.C. Huang, M. Glicksman, Overview 12: fundamentals of dendritic solidification-II development of sidebranch structure, Acta Metall. 29 (5) (1981) 717–734.
[104] E. Ben-Jacob, G. Deutscher, P. Garik, N.D. Goldenfeld, Y. Lareah, Formation of a dense branching morphology in interfacial growth, Phys. Rev. Lett. 57 (15) (1986) 1903.